A generalized approach to the vicarious calibration of multiple Earth observation sensors using hyperspectral data

P.M. Teillet[a],*, G. Fedosejevs[a], R.P. Gauthier[a], N.T. O'Neill[b],
K.J. Thome[c], S.F. Biggar[c], H. Ripley[d], A. Meygret[e]

[a]*Canada Centre for Remote Sensing, 588 Booth Street, Ottawa, Ontario, Canada K1A 0Y7*
[b]*CARTEL, Université de Sherbrooke, Sherbrooke, Québec, Canada J1K 2R1*
[c]*Optical Sciences Center, University of Arizona, Tucson, AZ, 85721-0094, USA*
[d]*Hyperspectral Data International, One Research Drive, Dartmouth, Nova Scotia, Canada B2Y 4M9*
[e]*Centre National d'Études Spatiales, BPI 811, 18, avenue Edouard Bélin, Toulouse Cedex 4 31401, France*

Abstract

The paper describes a new methodology that uses spatially extensive hyperspectral imagery as reference data to carry out vicarious radiometric calibrations for multiple satellite sensors. The methodology has been validated using data from a campaign at the Railroad Valley playa test site in Nevada in June 1998. The proof of concept has been further tested based on data acquisition campaigns at the Newell County rangeland test site in Alberta in August and October 1998. The rangeland test site in the Newell County region of Alberta is tested for its suitability as a calibration test site for satellite sensor systems. All three campaigns included ground-based measurements, satellite imagery, and airborne hyperspectral data. The airborne hyperspectral sensor data were acquired using the Airborne Visible and Infrared Imaging Spectrometer (AVIRIS) at Railroad Valley and the Compact Airborne Spectrographic Imager (*casi*) in all three campaigns. This paper describes the formulation and implementation of the new methodology, and radiometric calibration monitoring results obtained for five different sensors: NOAA-14 AVHRR, OrbView-2 SeaWiFS, SPOT-4 VGT, SPOT-1/2 HRV, and Landsat-5 TM. The results indicate that the nominal on-orbit radiometric calibrations of all the satellite sensors fit within their predicted uncertainties. The combination of both lower-reflectance and higher-reflectance test sites is shown to improve the quality of the calibration monitoring results. In particular, the combined QUASAR monitoring results obtained from the three airborne data acquisition days at the two test sites, encompassing five satellite sensors and a total of 40 spectral band cases, yield a correlation between QUASAR-based and nominal TOA radiances characterized by $y = 1.026x - 1.26$, and $r^2 = 0.990$. Temporal extensions of QUASAR data sets to calibrate satellite sensors imaging the test site one or more days away from the airborne data acquisition day yield mixed results. Crown Copyright © 2001 Published by Elsevier Science Inc. All rights reserved.

1. Introduction

Remote sensing calibration and validation (cal–val) are critical aspects of Earth observation measurements and the associated methods used to retrieve terrestrial parameters that are not compromised by sensor and data processing effects. The challenge is to ensure that the measurements and methods yield self-consistent and accurate geophysical parameters, even though the measurements are made with a variety of different satellite sensors under different observational conditions and the geophysical parameter retrieval methodologies vary.

Sensor radiometric calibration, the most fundamental part of the cal–val process, is a broad and complex field that imposes the greatest limitations on quantitative applications of remote sensing (Teillet, 1997; Teillet, Horler, & O'Neill 1997). The methods and instrumentation involved can be grouped into three domains (Dinguirard & Slater, 1999): on the ground prior to launch, onboard the spacecraft post-launch, and vicarious or indirect approaches using Earth scenes imaged in-flight. Whereas preflight methods encompass a vast array of painstaking sensor characterizations in the laboratory (e.g., Guenther et al., 1996) and occasionally outdoors (Biggar, Slater, Thome, Holmes, & Barnes, 1993), onboard and vicarious calibrations are devoted primarily to the monitoring of the radiometric responsivities or gain coefficients of sensor spectral bands over time. Advantages and disadvantages of these three categories of approaches have been discussed by Dinguirard and Slater (1999). In all

---

* Corresponding author. Tel.: +1-613-947-1251; fax: +1-613-947-1385.

E-mail address: phil.teillet@ccrs.nrcan.gc.ca (P.M. Teillet).

cases, the objective is traceability of data calibration accuracies to the International System of Units (SI) for science users and data products with consistent quality for the broader user community.

To date, Earth observation satellite sensors have been susceptible to significant post-launch changes in their performance characteristics. These changes arise as a result of many factors, including the rigours of the launch itself, the space environment in Earth orbit in general, the operating environment of the spacecraft, and aging of the sensors and their subsystems. Thus, even well-built, stable, and well-characterized sensors require evaluation and monitoring of changes in the months immediately following launch especially, but also over the lifetime of their operation. Although future Earth observation sensors will benefit from better technology, it is very likely that significant post-launch changes will still arise. Moreover, many forthcoming systems will have fewer, if any, onboard calibration systems in order to reduce costs. Hence, there will continue to be a need for several independent methodologies for the in-flight characterization of sensors to avoid or evaluate the presence of systematic errors. Equally important will be the operational infrastructure needed to integrate the results from these independent methodologies (Slater, Biggar, Palmer, & Thome, 1996) and make the resulting calibration coefficients available to data suppliers. The goal is to ensure that users benefit fully and in a timely fashion from the post-launch updates (Cabot, Hagolle, Ruffel, & Henry, 1999; Teillet et al., 1997).

This paper reports on experimental work to test the feasibility of using reference imaging spectrometer data (hereafter referred to as "hyperspectral" data) to carry out vicarious calibrations for multiple sensors. The domain of interest and applicability is that of optical sensors with spectral bands in the range encompassed by the "reference" hyperspectral sensor. The approach has the greatest potential for large footprint sensors (with spatial resolutions on the order of 1 km) since ground reference data are difficult to acquire over large areas, but it is equally applicable to small footprint sensors (with spatial resolutions on the order of tens of meters). Thus, the idea is to obtain reference data sets that are more generally applicable because of their more complete spectral coverage and more extensive spatial coverage compared to vicarious calibration methods used to date. Such an approach has the potential to provide more systematic vicarious calibration updates for numerous satellite sensor systems and it would represent an important step towards a cal−val infrastructure beneficial to mainstream users (Teillet et al., 1997). The approach is referred to as quality assurance and stability reference (QUASAR) monitoring.

1.1. The QUASAR monitoring concept

The QUASAR monitoring approach is a hybrid of reflectance-based and radiance-based methods that have been developed for the post-launch, vicarious radiometric calibration of satellite sensors (Slater et al., 1987; Slater, Biggar, Thome, Gellman, & Spyak, 1996; Thome, Markman, Barker, Slater, & Biggar, 1997). These methods predict the radiances at the top of the atmosphere (TOA) for a selected ground test site with the help of atmospheric radiative transfer code calculations. The reflectance-based approach typically uses ground-based measurements of surface reflectance and atmospheric characteristics to constrain these calculations. Test site coverage is focused on smaller areas (a few hundreds of meters) or a limited number of transects across larger areas. In the radiance-based approach, measurements of upwelling radiance from the test site are made using a well-calibrated, aircraft-based radiometer or spectrometer, usually not an imaging sensor. These radiances are then used to constrain the radiative transfer calculations to predict the radiances at the satellite sensor to be calibrated.

In the QUASAR method (Fig. 1), airborne hyperspectral image data are acquired over a spatially extensive test site and corrected for atmospheric effects to yield a surface spectral reflectance map. A further atmospheric computation is used to predict spectral radiances at the TOA, from which band-integrated radiances are obtained using relative spectral response profiles for the satellite sensor spectral bands being monitored.

The hyperspectral and spatially extensive nature of the resulting benchmark data set makes it possible to attempt vicarious calibrations for any sensor(s) with appropriate characteristics that imaged the test site on the same day, or within a day or two if atmospheric and surface conditions have not changed significantly. Appropriate sensors include any with footprints (i.e., pixel sizes) that fit comfortably within the test site and with one or more spectral bands encompassed by the wavelength coverage of the reference hyperspectral sensor. Spectral bands outside the wavelength range of the reference sensor can be monitored using interband relative calibration methods. Thus, the key application of QUASAR is the monitoring and updating of sensor radiometric calibration coefficients for many satellite sensors, including those with large footprint sizes, between infrequent high-accuracy updates.

A well-calibrated hyperspectral reference sensor in orbit would be ideal for this purpose, but the airborne approach is useful in the meantime for methodology prototyping and early operations while waiting for satellite hyperspectral sensors to become routinely available. Once a validated methodology becomes operational, the benchmark data sets could readily be disseminated to a wide audience on a rapid and frequent basis. Summary statistics could be made available as quickly as possible on an Internet Web site and the full data sets could be distributed at a later time on CD-ROM by purchase/subscription or by direct provision to stakeholders.

During the proof-of-concept phase, ground-based measurements of surface reflectance and atmospheric parameters are made for validation purposes. Operational QUASAR monitoring based on satellite hyperspectral reference data in
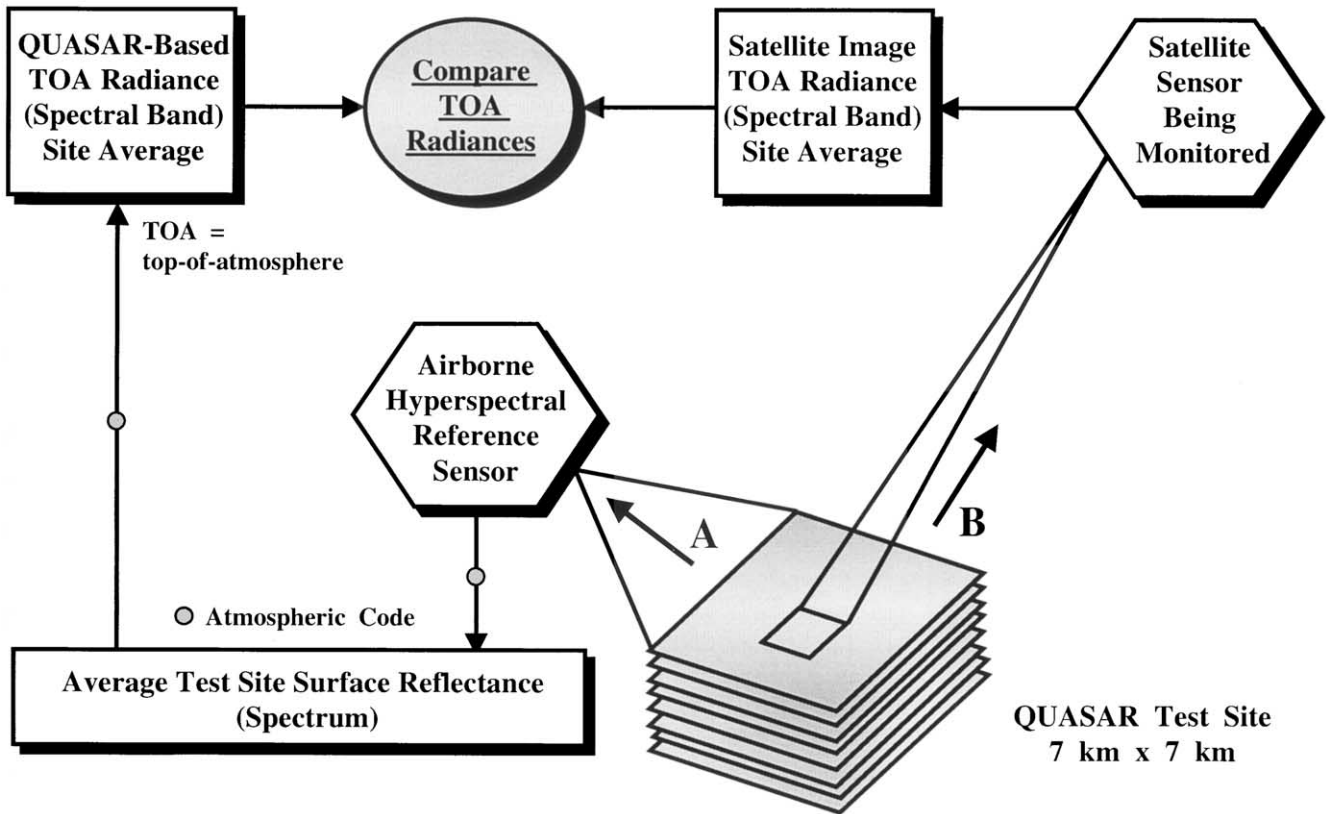
Fig. 1. The QUASAR concept for monitoring satellite sensor calibration, where TOA = top-of-atmosphere. The main results consist of comparisons between TOA radiances based on reference sensor data (A) and actual satellite sensor data (B).

the future could conceivably rely on sunphotometer and surface radiance measurements acquired by automated instrumentation. Because of the hyperspectral and spatially extensive nature of QUASAR data sets, the approach has the potential to eventually be adapted to the validation of geophysical and biophysical parameters derived from remotely sensed data.

This paper highlights the new QUASAR methodology, the data sets generated to date, and the first calibration monitoring results obtained for five well-known Earth observation satellite sensors. QUASAR monitoring data acquisition campaigns took place at the Railroad Valley playa test site in Nevada on June 17, 1998 and at the Newell County rangeland test site in Alberta on August 4, 1998 and October 4, 1998. Ground-based measurements, satellite imagery, and airborne hyperspectral data were acquired in all cases. The airborne imagery was obtained using the Compact Airborne Spectrographic Imager (*casi*) for all three campaigns and the Airborne Visible Infrared Imaging Spectrometer (AVIRIS) in addition for the Railroad Valley campaign. The ground-based measurements included spectral data obtained using the GER3700 spectrometer for all three campaigns and the ASD FieldSpec Pro FR spectrometer in addition for the Railroad Valley campaign.

The airborne hyperspectral data sets were used to generate radiometric calibration estimates for selected spectral bands of the Earth observation sensors that imaged the test sites on or near each of the three airborne data acquisition dates. The principal results consist of comparisons of TOA spectral band radiances predicted by QUASAR with nominal values obtained from the actual satellite sensor image data. The satellite sensors and the relevant spectral bands are as follows:

- National Oceanic and Atmospheric Administration's (NOAA) Advanced Very-High-Resolution Radiometer (AVHRR) (spectral band 1);
- Landsat Thematic Mapper (TM) (spectral bands 1–4);
- SPOT-1 and-2 Haute resolution visible (HRV) (spectral bands 1–3);
- SPOT-4 Vegetation (VGT) (spectral bands 1–3 (i.e., B0, B2, and B3)); and
- OrbView-2 Sea-viewing Wide-Field-of-View Sensor (SeaWiFS) (spectral bands 1–8).

Data sets both on and near the day of airborne data acquisition are included and provide challenging scenarios for an initial test of the feasibility of the QUASAR monitoring approach. This is in keeping with the philosophy of the QUASAR experiment to relax the constraints on the generation of benchmark data sets in favour of more frequent radiometric calibration updates.

2. Test sites

Vicarious calibration test sites are usually flat, homogeneous areas located in desert regions, such as the southwest United States, central Australia, northern Africa, and China's Gobi desert, for example. Desert regions have bright surfaces, a low probability of interference from clouds, and generally low aerosol loading (especially for sites at higher elevations), all factors that decrease calibration uncertainties due to the atmospheric characterization involved in the method. Perhaps, the best known calibration test site is Chuck Site in the alkali gypsum flats at White Sands, NM. It has been used for radiometric calibration of the Landsat TM and SPOT HRV sensors, primarily (Slater et al., 1987; Thome et al., 1997), but also for AVHRR series of satellite sensors (Teillet et al., 1990).

For the QUASAR monitoring concept, test sites should also be large enough (5–10 km across, ideally) for use with respect to many satellite sensors, including those with large footprint sizes. Independent test sites with lower reflectances than the usual desert sites would also be valuable because multiple reflectances make it possible to establish a radiometric calibration curve over a larger range of target brightness.

2.1. Railroad Valley playa, Nevada

Central Nevada contains many dry lake playas of various sizes and two have received increasing attention as calibration sites by the international community: the Lunar Lake playa and the Railroad Valley playa. Lunar Lake playa is smaller (approximately 2×3 km²) and more suitable for the calibration of high-resolution sensors such as Landsat TM, SPOT HRV, and Earth Observing System (EOS) Advanced Spaceborne Thermal Emission and Reflection Radiometer (ASTER), for example. The Railroad Valley playa extends over a larger area (approximately 12×12 km²) and lends itself better to the calibration of large footprint sensors such as NOAA-14 AVHRR, SPOT-4 VGT, and OrbView-2 SeaWiFS, as well as the EOS MODerate resolution Imaging Spectroradiometer (MODIS), Envisat MEdium Resolution Imaging Spectrometer (MERIS), and ADEOS-2 Global Imager (GLI), for example.

The Railroad Valley playa is situated in central Nevada at 38°28′N and 115°41′W and at an elevation of 1435 m above sea level (ASL) (Table 1). Its larger area compared to Lunar Lake playa makes it a better choice for QUASAR monitoring studies. It is very homogeneous and consists of compacted clay-rich lacustrine deposits forming a relatively smooth surface compared to most land covers. Currently, no soils or geology maps have been obtained for the area. Three weather stations are situated in the general vicinity of the playa. One is located near Twin Springs Ranch about 40 km southwest of Railroad Valley. The others are at the Tonopah airport some 145 km southwest and at the Ely airport approximately 155 km northeast. The precipitation data recorded at these stations reveal a substantial variation in amounts of rainfall. Because of the mountainous terrain in the region, the most reliable information for the immediate area of the test site would be in situ field observations.

The Railroad Valley playa in Nevada (hereafter referred to as RVPN) has a growing history of international use as a

Table 1
Characteristics of the Newell County rangeland test site in Alberta and the Railroad Valley playa test site in Nevada

Feature	Newell county site	Railroad Valley playa site
Mean terrain elevation	750 m ASL	1435 m ASL
Terrain character	flat to sloping or long rolling	flat
	<1% water incursions	seasonal standing water
	(<100 m in size)	primarily in peripheral areas
	some petroleum	
	development infrastructure	
Airborne *casi* coverage block size (1998)	7 km (E−W) × 7 km (N−S)	7 km (NW−SE) × 7 km (NE−SW)
Airborne *casi* coverage location corners (1998)	north latitude 50°19′38″	north latitude 38°32′03″
	5,575,030 m Northing	4,265,664 m Northing
	west longitude 111°41′17″	west longitude 115°40′38″
	451,030 m Easting	615,300 m Easting
	north latitude 50°19′38″	north latitude 38°29′08″
	5,574,970 m Northing	4,260,361 m Northing
	west longitude 111°35′24″	west longitude 115°37′36″
	458,030 m Easting	619,771 m Easting
	north latitude 50°15′52″	north latitude 38°26′45″
	5,568,030 m Northing	4,255,867 m Northing
	west longitude 111°41′17″	west longitude 115°41′19″
	450,970 m Easting	614,422 m Easting
	north latitude 50°19′38″	north latitude 38°29′40″
	5,567,970 m Northing	4,261,217 m Northing
	west longitude 111°35′24″	west longitude 115°44′23″
	457,970 m Easting	609,928 m Easting

Fig. 2. The Railroad Valley playa as imaged by SPOT-1 HRV on June 18, 1998 (north is to the top). HRV spectral bands 1, 2, and 3 are shown in red, green, and blue, respectively. The red box outlines the RVPN test site, which is 7×7 km^2 in extent. The location of the 100×100 m^2 ground validation site is indicated by the small red square within the test site.

test site for vicarious calibration and it serves as a good setting for QUASAR methodology evaluation. It is conceivable that it could serve as an ongoing QUASAR monitoring site to provide a periodic tie-in of the approach to international methodology standards and radiometric scales. Routine sensor performance monitoring could make use of a variety of test sites around the world, including more common sites with lower reflectances than desert sites.

2.2. Newell County rangeland site, Alberta

Potentially uniform sites in the Canadian prairies include croplands and rangeland. While croplands tend to be very flat and uniform within fields, any given crop type is usually limited to 1.6×1.6 km^2 or less in size and such land cover exhibits high rates of phenological change at times. Native rangeland provides slowly varying phenology and relatively uniform vegetation cover over large tracts of land. The utilization of flatter and more productive rangeland for grazing, and the incursion of petroleum exploration into unspoiled rangeland do diminish the chances of finding extended regions of undisturbed and flat native rangeland. Nevertheless, much of the disturbance due to exploration is transient and localized, such that there is little long-term change to the rangeland overall.

Based on visual examination of NOAA AVHRR imagery, aerial photographs, topographic maps, and field

reconnaissance, two rangeland sites in southeastern Alberta were selected for initial QUASAR studies. After the first data acquisition mission (Teillet, Fedosejevs, & Gauthier, 1998), only the rangeland site in Newell County, Alberta, was kept for future use. The Newell County rangeland area of interest is located northwest of Medicine Hat, Alberta at 50°18′N and 111°38′W and at an elevation of 750 m ASL. Additional site descriptors are given in Table 1. Given its reasonable proximity to urban areas from which hyperspectral sensors can be flown (a few hundred kilometers) and its lower reflectance compared to desert sites, the Newell County rangeland in Alberta (hereafter referred to as NCRA) has the potential to serve as a routine test site for interim performance monitoring of satellite sensors.

2.3. Determination of prime test site location and size

Radiometric uniformity studies were used to determine the location and size of a primary test site in the Railroad Valley and Newell County areas (Teillet, Fedosejevs, Gauthier, & Schowengerdt, 1998). Image data at 1-km spatial scale were simulated from SPOT HRV imagery in order to characterize radiometric uniformity with the calibration of large footprint sensors in mind. For single-date 1-km images of both the RVPN area and the NCRA area, it was found that there are windows 7×7 km^2 in size that have coefficients of variation less than or equal to 3% in all three HRV spectral
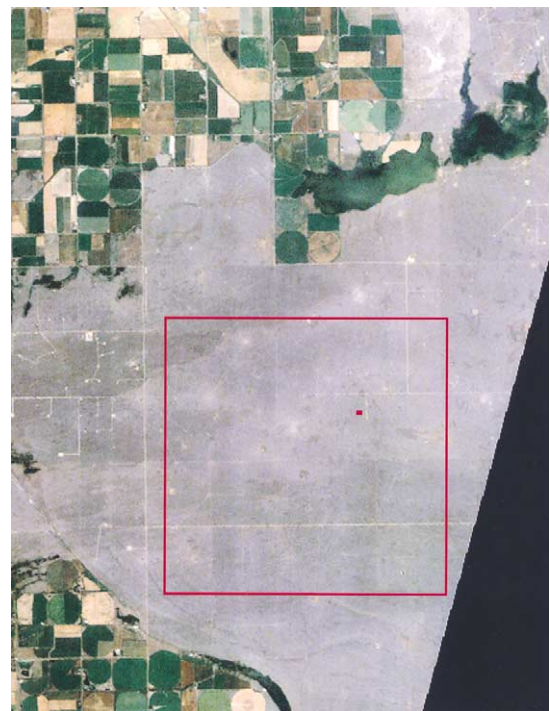

Fig. 3. The Newell County rangeland area as imaged by Landsat-5 TM on August 8, 1998. TM spectral bands 1, 2, and 3 are shown in blue, green, and red, respectively. The red box outlines the NCRA test site, which is 7×7 km^2 in extent. The location of the 100×100 m^2 ground validation site is indicated by the small red square within the test site.

bands. For a selected prime site of 7×7 km^2 at each location, descriptive statistics from the 1-km data indicate that both sites could be equally useful as vicarious calibration sites for large footprint sensors (Teillet, Fedosejevs, Gauthier, et al., 1998). These 7×7 km^2 prime test sites were used in this study (Figs. 2 and 3). Fig. 3 shows that the rangeland surface, although heterogeneous at a detailed scale (Fig. 4), nevertheless exhibits a reasonable degree of uniformity at the pixel scales of small and large footprint sensors.

However, radiometric uniformity characteristics of subareas within the prime sites at both locations indicate that test site sizes of 5×5 km^2 may have to be considered in the future if greater uniformity is needed. For the images used in the aforementioned uniformity study, such site dimensions

would yield coefficients of variation of 2% in all three HRV spectral bands. Test sites 5×5 km^2 in size could preclude the use of pixels at very large off-nadir angles in vicarious calibration schemes. Further data analyses and experience with the test sites should lead to a better understanding of seasonal characteristics, directional reflectance properties, and radiometric uniformity at finer spatial scales.

3. Airborne and ground-based data acquisition

The QUASAR data sets used in this study are summarized in Table 2 and involve three measurement campaigns (one at RVPN and two at NCRA).
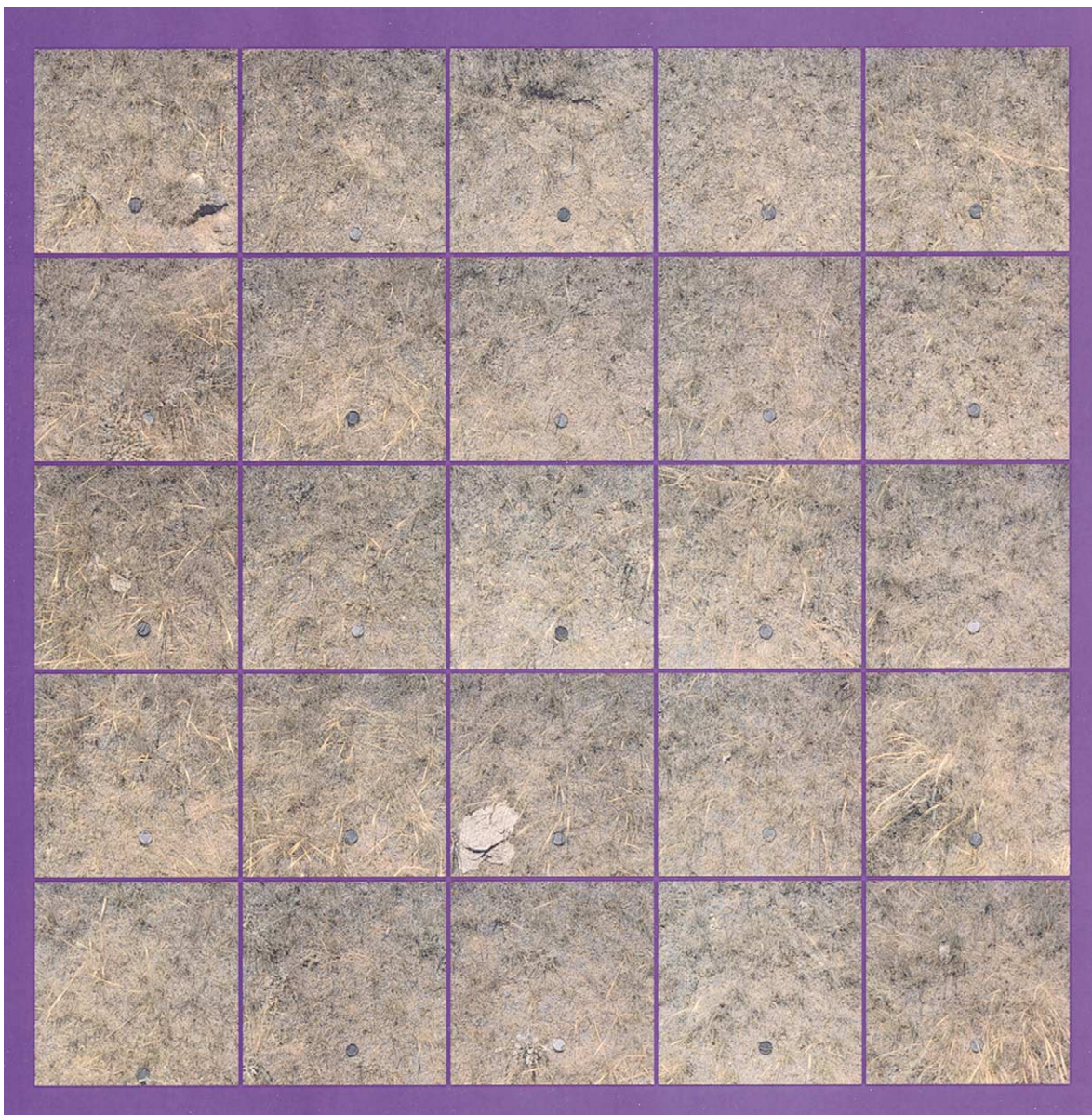

Fig. 4. Vertical 35-mm photography of the Newell County rangeland surface. The photographs were taken approximately 1.2 m above ground at 25 of the locations within the 100×100 m^2 ground validation site where surface spectral reflectance data were acquired. The black circular object visible in most of the photographs is a camera lens cap.

Table 2
QUASAR data summary for the RVPN test site, Nevada, in June 1998 and the NCRA test site, Alberta, in August and October 1998

	June							August						October				
Data sets	14	17	18	19	20	21	22	4	6	7	8	9	10	3	4	5	6	8
Sunphotometers																		
Microtops-II	•				•													
Reagan	•																	
Ground spectrometers																		
GER 3700	•										•				•			
FieldSpec	•																	
Airborne sensors																		
casi	•							•							•			
AVIRIS	•																	
Satellite sensors																		
NOAA-14 AVHRR	•	•	•(2)	•(2)	•	•	•	•	•	•		•	•	•	•		•	•
OrbView-2 SeaWiFS	•	•							•		•		•	•	•		•	•
SPOT-4 VGT	•								•	•					•	•		
SPOT-1 HRV				•														
SPOT-2 HRV												•				•		
Landsat-5 TM	•											•				•		

3.1. Airborne hyperspectral data acquisition

The airborne imagery was obtained using *casi* for all three campaigns and AVIRIS in addition for the Railroad Valley campaign. AVIRIS is known to be a well-calibrated sensor and it has been a key component of the QUASAR methodology validation. The advantages of using *casi* are that it is relatively easy to use on light aircraft platforms, it costs much less to deploy than most other imaging spectrometer systems, and it has considerable flexibility in terms of selectable spatial and spectral modes of data acquisition. The disadvantages of *casi* are that it covers only the visible and near-infrared spectral regions and any geometric rectification of interest is non-trivial because of aircraft motion effects. Data acquisition by the Shortwave-Infrared (SWIR) Full Spectrum Imager (SFSI) (Neville, Rowlands, Marois, & Powell, 1995) could also be considered in the future, although, unlike the *casi*, only one such system exists and its regular availability is uncertain. An alternative would be to bore-site a visible, near-infrared and shortwave-infrared spectrometer with the *casi* to acquire at least a nadir profile in the SWIR (P. Slater, personal communication).

For the Railroad Valley test site, the AVIRIS and *casi* airborne missions were flown on June 17, 1998. The AVIRIS data acquisition captured the entire RVPN test site within one flight line (swath width of 11 km) from a flight altitude of 20.8 km ASL (19.3 km above ground level) such that the spatial resolution of the data is approximately 17.5

m. AVIRIS has a spectral range extending from 0.4 to 2.5 µm with 224 spectral bands. The *casi* flight altitude was 3400 m ASL (1965 m above ground level) such that the spatial resolution of the data is approximately 2.6 m.

For the Newell County test site, the *casi* airborne missions were flown on August 4, 1998 and October 4, 1998 with a flight altitude of 3000 m ASL (2245 m above ground level) such that the spatial resolution of the data is approximately 3 m. Other characteristics of the *casi* airborne data acquisitions for the 1998 missions were:

- 11 or more parallel flight lines providing wall-to-wall coverage of each 7×7 km² test site;
- lateral overlap of 30% of the swath width between flight lines;
- spectral range extending from 0.450 to 0.960 µm with 96 spectral bands; and
- scan-angle range of $+22°$ to $-15°$ with respect to nadir.

3.2. Ground-based spectrometer measurements

A 100×100 m² ground validation site within the 7×7 km² test site was selected at both QUASAR test sites for ground-based measurements. In all cases, these measurements included GER3700 spectrometer measurements made over the surface and over a Labsphere Spectralon reflectance panel to generate surface reflectances for use in validating surface reflectances retrieved from the airborne hyperspectral imagery. At the RVPN test site, the ground-based measurements also included FieldSpec spectrometer measurements. The FieldSpec measurements were made over the playa at a location near the ground validation site and over a Spectralon reflectance panel to generate surface reflectances for use as an independent validation of surface reflectances retrieved from the GER spectrometer and the airborne hyperspectral imagery. Both of the aforementioned reflectance panels were calibrated radiometrically and characterized for bidirectional reflectance properties in the laboratory at the University of Arizona.

The GER3700 is a ground-based spectroradiometer that covers the wavelength range from 0.4 to 2.45 µm. A $10°$ field-of-view was used in this experiment. The optical system consists of three spectrometers and three detector arrays. The first spectrometer uses a diffraction grating and a 512-element silicon detector array to capture the wavelength range from 0.4 to 1.05 µm, which more than covers the spectral domain of interest in the *casi*-based proof-of-concept phase of QUASAR. This spectrometer's spectral bandwidth is 0.0015 µm (1.5 nm).

The FieldSpec Pro FR spectrometer has a $0.35-2.5$ µm spectral range. It operates with a fiber optic cable 1.4 m in length with a $25°$ field-of-view. Three spectrometers are used to cover the full spectral range. The first spectrometer uses a 512-element photo-diode array and a holographic reflective grating to cover the wavelength range from 0.35

to 1.0 μm. This spectrometer has a sampling interval of 0.0014 μm (1.4 nm) and the spectral resolution is 0.003 μm at 0.7 μm.

The ground validation site was subdivided into quadrants and sub-quadrants for a total of 16 cells (Fig. 5). GER3700 spectrometer data were acquired in each of the cells in turn. The reflectance panel was deployed sequentially in the centre of each of the four main quadrants and used in conjunction with the spectrometer measurements for the four adjacent cells. The spectrometer measurements were made using nadir-viewing geometry at 10 locations per cell distributed spatially in semi-random fashion and the set of 10 bracketed by reflectance panel measurements. The spectrum for each of the 10 locations is an average of 10 GER3700 scans.

3.3. Sunphotometer measurements

Sunphotometer measurements were made from the centre of the surface grid using a handheld, calibrated Microtops-II sunphotometer during the satellite and aircraft sensor overpasses. The sunphotometer has built-in processing capability to compute a variety of atmospheric parameters at several wavelengths from instantaneous solar disk readings. The resulting data were used to obtain atmospheric aerosol optical depth at 0.550 μm (AOD550). For the RVPN test site
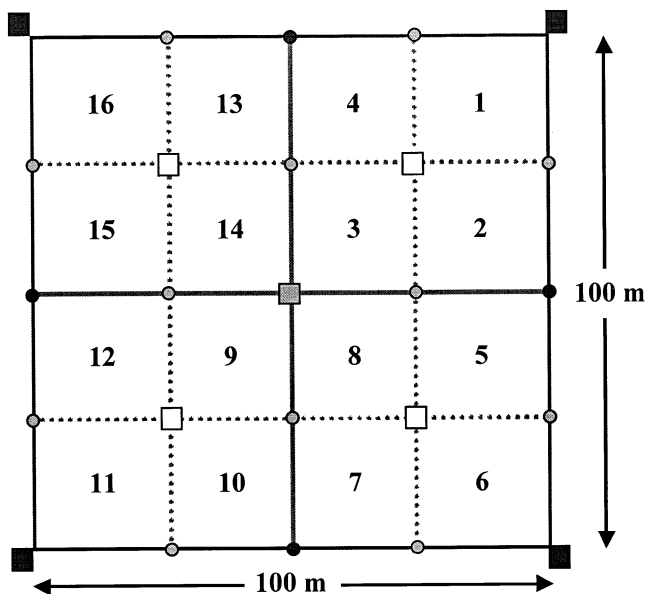

Fig. 5. Ground-based spectrometer data acquisition pattern used at the QUASAR test sites as discussed in the text. GER3700 spectrometer data were acquired in each of the 16 cells in the indicated numerical order. The deployment locations for the Labsphere Spectralon reflectance panel are indicated by white squares. Sun photometer measurements were made from the centre of the grid at the location indicated by the gray square. The black and gray circles represent flag markers deployed as visual reference points to help outline the cells during the surface measurement process. Blue tarpaulins were deployed in at least two of the four corners to serve as markers for the RVPN test site.

on June 17, 1998, this yielded a characteristic value of AOD550 = 0.04. For the NCRA test site, the characteristic value of AOD550 on August 4, 1998 was 0.09. Despite plans to the contrary, sunphotometer measurements were not available during the October data acquisition campaign. Atmospheric conditions were clear and a value of 0.05 was assumed for AOD550.

At the RVPN test site, sunphotometer measurements were also made using a well-calibrated, tripod-mounted Reagan solar radiometer. A comparison of Microtops-II and Reagan sunphotometer measurements over the course of several days at the playa showed differences in retrieved AOD550 averaging 0.01 and not exceeding 0.03.

3.4. Satellite data

For the RVPN test site, near-coincident satellite sensor imagery was acquired on the *casi* and AVIRIS flight day, June 17, 1998, by NOAA-14 AVHRR, OrbView-2 Sea-WiFS, and SPOT-4 VGT (Table 2). SPOT-1 HRV data were acquired on the next day, whereas Landsat-5 TM data were acquired 3 days prior to the airborne data acquisition day. Other AVHRR and SeaWiFS data were also acquired within a few days of June 17.

For the NCRA test site, near-coincident satellite sensor imagery was acquired on the *casi* flight day, August 4, 1998, by NOAA-14 AVHRR and OrbView-2 SeaWiFS (Table 2). SPOT-4 VGT and other AVHRR and SeaWiFS data were also acquired within a few days of August 4. SPOT-2 HRV and Landsat-5 TM image data were acquired 3 and 4 days, respectively, after the airborne data acquisition day. For the October NCRA data acquisition campaign, near-coincident satellite sensor imagery was acquired on the *casi* flight day, October 4, 1998, by NOAA-14 AVHRR, OrbView-2 Sea-WiFS, SPOT-4 VGT, Landsat-5 TM, and SPOT-2 HRV. Other AVHRR, VGT, and SeaWiFS data were also acquired within a few days of October 4.

The wavelength coverage provided by the airborne hyperspectral *casi* data is such that QUASAR results can be generated for AVHRR spectral band 1, SeaWiFS spectral bands 1−8, VGT spectral bands 1−3, HRV spectral bands 1−3, and TM spectral bands 1−4. The central wavelengths and integrated bandpasses for these spectral bands are given in Tables 3−6.

4. Data processing and analysis

The QUASAR data flow scheme is summarized in Fig. 6, which is a more detailed version of the conceptual data flow depicted in Fig. 1. A few general points should be made before describing the data processing and analysis steps individually. Multiple flight line processing steps pertain to *casi* data only since the AVIRIS data involve one flight line. Unless otherwise indicated, all other processing steps are applied to both *casi* and AVIRIS data sets, although the text

Table 3
QUASAR parameters and radiometric calibration results for the RVPN test site (June 17, 1998)[a]

	NOAA-14 AVHRR	OrbView-2 SeaWiFS	OrbView-2 SeaWiFS	OrbView-2 SeaWiFS	OrbView-2 SeaWiFS	OrbView-2 SeaWiFS	OrbView-2 SeaWiFS	OrbView-2 SeaWiFS	OrbView-2 SeaWiFS	SPOT-4 VGT	SPOT-4 VGT	SPOT-4 VGT
Spectral band	1	1	2	3	4	5	6	7	8	1 (B0)	2 (B2)	3 (B3)
Central wavelength (μm)	0.633	0.412	0.443	0.490	0.510	0.555	0.67	0.765	0.865	0.445	0.670	0.825
Integrated bandpass (μm)	0.1334	0.0151	0.0161	0.0173	0.0182	0.0161	0.0167	0.0348	0.0354	0.0409	0.0798	0.1198
Exo-atmospheric solar irradiance	1561.5	1709.5	1909.7	1932.8	1892.3	1878.8	1536.3	1213.7	978.1	1962.5	1547.4	1047.7
Time (UTC)	21:25	20:50	20:50	20:50	20:50	20:50	20:50	20:50	20:50	18:01	18:01	18:01
Solar distance (AU)	1.0160	1.0160	1.0160	1.0160	1.0160	1.0160	1.0160	1.0160	1.0160	1.0160	1.0160	1.0160
Solar zenith angle (°)	26.3	20.7	20.7	20.7	20.7	20.7	20.7	20.7	20.7	26.5	26.5	26.5
Solar azimuth angle (°)	242.4	228.0	228.0	228.0	228.0	228.0	228.0	228.0	228.0	117.2	117.2	117.2
View zenith angle (°)	43.9	58.7	58.7	58.7	58.7	58.7	58.7	58.7	58.7	43.0	43.0	43.0
View azimuth angle (°)	79.0	278.8	278.8	278.8	278.8	278.8	278.8	278.8	278.8	101.0	101.0	101.0
Rayleigh optical depth	0.0457	0.2686	0.1955	0.1308	0.1115	0.0790	0.0369	0.0215	0.0131	0.1743	0.0396	0.0157
Aerosol optical depth	0.0343	0.0559	0.0516	0.0466	0.0447	0.0406	0.0326	0.0275	0.0235	0.0500	0.0331	0.0248
BRF factor for satellite sensor case	0.95	0.88	0.88	0.88	0.88	0.88	0.88	0.88	0.88	1.02	1.02	1.02
Test site %RHO from QUASAR (TQ)	40.4	20.0	26.3	33.1	35.0	38.8	43.3	45.8	46.1	28.6	43.1	46.1
Val site %RHO from ASD (G)	40.0	21.7	26.4	31.4	33.3	38.7	43.0	45.5	46.0	28.1	42.6	46.0
ΔRHO=% (TQ − G)/G	1.0%	− 7.8%	− 0.5%	5.6%	5.0%	0.2%	0.6%	0.7%	0.2%	1.9%	1.1%	1.2%
Val site %RHO from QUASAR (VQ)	40.0	20.1	26.2	32.8	34.7	38.4	42.9	45.4	45.6	28.5	42.7	45.5
ΔRHO=% (VQ − G)/G	0.0%	− 7.3%	− 0.8%	4.8%	4.0%	− 0.7%	− 0.3%	− 0.2%	− 1.0%	1.4%	0.2%	0.0%
Average image DSL for test site	259.5	830.0	831.0	834.9	835.8	838.7	847.7	848.8	853.5	646.2	539.8	581.4
Nominal post-launch cal gain	1.435									3.664	3.202	3.258
Nominal post-launch cal gain factor										1	1	1.4142
Nominal post-launch cal offset	41									0	0	0
TOAL^* from nominal PLC (N)	151.7	139.1	163.7	165.2	165.0	170.7	163.9	121.0	110.7	176.4	168.6	126.2
TOAL^* from QUASAR PLC (Q)	162.8	136.5	158.3	174.9	173.0	173.7	161.3	117.2	113.3	181.7	177.8	131.0
ΔTOAL^*=% (Q − N)/N	7.3%	− 1.8%	− 3.3%	5.8%	4.8%	1.8%	− 1.5%	− 3.2%	2.3%	3.0%	5.5%	3.8%

DSL units are image counts; radiances L^* units are W/(m^2 sr μm); irradiances units are W/(m^2 μm); gain units are counts/radiance.

Railroad Valley test site latitude = 38°28′52″; longitude = − 115°39′47″; elevation = 1435 m.

Atmospheric parameters: ozone content (cm atm) = 0.344; water vapour content (g/cm^2) = 1.10; AOD550 = 0.041.

[a] UTC = coordinated universal time; AU = astronomical units; RHO = surface reflectance; DSL = digital signal level; PLC = post-launch calibration; TOA = top of atmosphere.

Table 4
QUASAR parameters and radiometric calibration results for the NCRA test site (August 4, 1998)[a]

	NOAA-14 AVHRR	OrbView-2 SeaWiFS	OrbView-2 SeaWifS	OrbView-2 SeaWiFS	OrbView-2 SeaWiFS	OrbView-2 SeaWiFS	OrbView-2 SeaWiFS	OrbView-2 SeaWiFS	OrbView-2 SeaWifS
Spectral band	1	1	2	3	4	5	6	7	8
Central wavelength (μm)	0.633	0.412	0.443	0.490	0.510	0.555	0.67	0.765	0.865
Integrated bandpass (μm)	0.1334	0.0151	0.0161	0.0173	0.0182	0.0161	0.0167	0.0348	0.0354
Exo-atmospheric solar irradiance	1561.5	1709.5	1909.7	1932.8	1892.3	1878.8	1536.3	1213.7	978.1
Time (UTC)	20:59	20:24	20:24	20:24	20:24	20:24	20:24	20:24	20:24
Solar distance (AU)	1.0145	1.0145	1.0145	1.0145	1.0145	1.0145	1.0145	1.0145	1.0145
Solar zenith angle (°)	37.5	34.7	34.7	34.7	34.7	34.7	34.7	34.7	34.7
Solar azimuth angle (°)	215.8	201.9	201.9	201.9	201.9	201.9	201.9	201.9	201.9
View zenith angle (°)	35.4	31.0	31.0	31.0	31.0	31.0	31.0	31.0	31.0
View azimuth angle (°)	79.0	249.9	249.9	249.9	249.9	249.9	249.9	249.9	249.9
Rayleigh optical depth	0.0754	0.2925	0.2122	0.1419	0.1211	0.0860	0.0402	0.0234	0.0142
Aerosol optical depth	0.319	0.1227	0.1132	0.1022	0.0981	0.0891	0.0715	0.0604	0.0515
BRF factor for satellite sensor case	0.88	1.20	1.20	1.20	1.20	1.20	1.20	1.20	1.20
Test site %RHO from QUASAR (TQ)	8.1	2.3	3.7	5.3	5.9	6.9	7.8	15.1	17.8
Val site %RHO from GER (G)	8.5	3.7	4.5	5.4	5.9	7.5	8.2	18.0	20.8
ΔRHO=%(TQ − G)/G	− 5.2%	− 37.8%	− 16.9%	− 1.3%	0.0%	− 8.3%	− 4.5%	− 15.9%	− 14.1%
Val site %RHO from QUASAR (VQ)	8.0	2.1	3.8	5.2	5.7	7.1	7.6	17.4	19.7
ΔRHO=% (VQ − G)/G	− 5.8%	− 43.2%	− 14.6%	− 3.9%	− 2.6%	− 4.4%	− 6.9%	− 3.1%	− 5.0%
Average image DSL for test site	88.9	566.8	573.3	645.7	693.0	795.0	795.5	808.4	813.1
Nominal post-launch cal gain	1.435								
Nominal post-launch cal offset	41								
TOAL* from nominal PLC (N)	33.4	75.1	71.9	62.3	58.7	56.9	50.0	53.6	53.4
TOAL* from QUASAR PLC (Q)	40.8	64.4	70.4	60.6	64.6	52.1	48.4	55.7	55.9
ΔTOAL*=%(Q − N)/N	22.3%	− 14.3%	− 2.2%	− 2.7%	10.0%	− 8.4%	− 3.2%	3.8%	4.6%

DSL units are image counts; radiances L* units are W/(m² sr μm); irradiances units are W/(m² μm); gain units are counts/radiance.

Newell County test site latitude = 50°18′20″; longitude = − 111°37′32″; elevation = 750 m.

Atmospheric parameters: ozone content (cm atm) = 0.319; water vapour content (g/cm²) = 2.2; AOD550 = 0.09.

[a] UTC = coordinated universal time; AU = astronomical units; RHO = surface reflectance; DSL = digital signal level; PLC = post-launch calibration; TOA = top of atmosphere.

concentrates primarily on *casi* data processing. Each flight line of airborne *casi* imagery is processed separately through the surface reflectance retrieval stage. This allows for roll and scan-angle corrections to be applied. It should also be noted that, in order to optimize processing time, as much of the processing as possible is done with spatially averaged spectral data, i.e., scan lines are averaged and later in the data flow pixels are averaged, instead of processing all pixels in a flight line image segment. In an operational QUASAR monitoring scenario, once calibration update estimates have been derived for the satellite sensors being monitored, surface reflectance maps and other products for the full spatial coverage of the test site can be generated for later distribution.

4.1. Surface spectral reflectance retrieval

The first step in the processing of each *casi* flight line image is a roll correction to remove the most severe effect of aircraft attitude variations. Corrections for aircraft pitch and yaw variations are not yet part of the processing scheme. The next step is to extract the portion of each flight line image that covers the test site, hereafter referred to as a flight line image segment. This extraction process allows for the 30% overlap between flight lines, with the result that the *casi* scan-angle range is reduced from + 22/ − 15° to + 16/

− 10° with respect to nadir. The scan lines of the flight line image segment are then averaged to form an average scan-angle image whose dimensions are 212 pixels × 1 line × 96 spectral bands. This procedure can be represented by the following equation (Eq. (1)):

$$\overline{L_{ikl}^*}(\theta_{s,l}, \theta_v, \Delta\phi_l) = \frac{1}{J}\sum_{j=1}^{J} L_{ijkl}^*(\theta_{s,l}, \theta_v, \Delta\phi_l), \qquad (1)$$

where L* = apparent radiance at (*casi*) sensor altitude; $\overline{L*}$ = apparent radiance at (*casi*) sensor altitude averaged over image lines; θ_s = solar zenith angle; θ_v = view zenith angle; $\Delta\phi$ = relative azimuth angle between solar azimuth and view azimuth directions; i = image pixel coordinate; j = image line coordinate; k = spectral band index; l = flight line segment index; and J = total number of image lines in a flight line segment.

An atmospheric correction is then performed to retrieve surface spectral reflectance as a function of view angle from the average scan-angle image obtained from the given flight line segment. The expression "view angle" is used in connection with surface reflectance, whereas the expression "scan angle" is used in connection with data at aircraft altitude. The Imaging Spectrometer Data Analysis System (ISDAS) (Staenz, Szeredi, & Schwarz, 1998) at the Canada Centre for Remote Sensing was used to carry out the

Table 5a
QUASAR parameters and radiometric calibration results for the NCRA test site (October 4, 1998)[a]

	NOAA-14 AVHRR	OrbView-2 SeaWiFS	OrbView-2 SeaWiFS	OrbView-2 SeaWiFS	OrbView-2 SeaWiFS	OrbView-2 SeaWiFS	OrbView-2 SeaWiFS	OrbView-2 SeaWiFS	OrbView-2 SeaWiFS
Spectral band	1	1	2	3	4	5	6	7	8
Central wavelength (μm)	0.633	0.412	0.443	0.490	0.510	0.555	0.67	0.765	0.865
Integrated bandpass (μm)	0.1334	0.0151	0.0161	0.0173	0.0182	0.0161	0.0167	0.0348	0.0354
Exo-atmospheric solar irradiance	1561.5	1709.47	1909.7	1932.8	1892.3	1878.8	1536.3	1213.7	978.1
Time (UTC)	21:27	19:45	19:45	19:45	19:45	19:45	19:45	19:45	19:45
Solar distance (AU)	1.0001	1.0004	1.0004	1.0004	1.0004	1.0004	1.0004	1.0004	1.0004
Solar zenith angle (°)	61.7	55.2	55.2	55.2	55.2	55.2	55.2	55.2	55.2
Solar azimuth angle (°)	218.0	189.4	189.4	189.4	189.4	189.4	189.4	189.4	189.4
View zenith angle (°)	12.3	36.5	36.5	36.5	36.5	36.5	36.5	36.5	36.5
View azimuth angle (°)	77.0	132.0	132.0	132.0	132.0	132.0	132.0	132.0	132.0
Rayleigh optical depth	0.0419	0.2925	0.2129	0.1424	0.1214	0.0860	0.0402	0.0234	0.0142
Aerosol optical depth	0.319	0.0682	0.0629	0.0568	0.0545	0.0495	0.0397	0.0325	0.0286
BRF factor for satellite sensor case	0.88	1.29	1.29	1.29	1.29	1.29	1.29	1.29	1.29
Test site %RHO from QUASAR (TQ)	9.6	2.7	4.7	6.4	6.8	7.9	9.8	15.3	17.5
Val site %RHO from GER (G)	10.3	4.7	5.8	6.9	7.3	8.5	10.4	16.6	19.3
$\Delta RHO = \%(TQ - G)/G$	−6.4%	−44.1%	−19.7%	−7.1%	−6.8%	−7.8%	−5.9%	−7.8%	−9.5%
Val site %RHO from QUASAR (VQ)	10.1	2.7	4.9	6.7	7.2	8.4	10.1	17.1	18.7
$\Delta RHO = \%(VQ - G)/G$	−2.1%	−43.7%	−15.9%	−2.5%	−1.8%	−2.1%	−2.7%	2.9%	−2.9%
Average image DSL for test site	78.1	482.10	487.80	555.80	584.60	649.30	792.20	798.70	801.40
Nominal post-launch cal gain	1.428								
Nominal post-launch cal offset	41								
TOA L^* from nominal PLC (N)	26.0	63.8	61.6	53.6	49.8	45.7	42.8	39.9	39.3
TOA L^* from QUASAR PLC (Q)	25.0	54.2	59.4	49.9	53.5	43.7	42.0	42.1	42.0
Δ TOA $L^* = \%(Q - N)/N$	−3.7%	−15.1%	−3.6%	−6.9%	7.5%	−4.4%	−1.9%	5.6%	6.8%

[a] UTC = coordinated universal time; AU = astronomical units; RHO = surface reflectance;
   DSL = digital signal level; PLC = post-launch calibration; TOA = top of atmosphere.
   DSL units are image counts; radiances L^* units are W/(m² sr μm); irradiances units are W/(m² μm); gain units are counts/radiance.
   SPOT-4 VGT image data were provided in calibrated units, not DSL.
   Newell County test site latitude = 50°18′20′′; longitude = −111°37′32′′; elevation = 750 m.
   Atmospheric parameters: ozone content (cm atm) = 0.319; water vapour content (g/cm²) = 1.35; AOD550 = 0.05.

Table 5b
QUASAR parameters and radiometric calibration results for the NCRA test site (October 4, 1998)[a]

	SPOT-4 VGT	SPOT-4 VGT	SPOT-4 VGT	SPOT-2 HRV	SPOT-2 HRV	SPOT-2 HRV	Landsat-5 TM	Landsat-5 TM	Landsat-5 TM	Landsat-5 TM
Spectral band	1 (B0)	2 (B2)	3 (B3)	1	2	3	1	2	3	4
Central wavelength (μm)	0.445	0.670	0.825	0.549	0.653	0.84	0.4863	0.5706	0.6607	0.8382
Integrated bandpass (μm)	0.0409	0.0798	0.1198	0.0879	0.0644	0.1005	0.0610	0.0763	0.0657	0.1206
Exo-atmospheric solar irradiance	1962.5	1547.4	1047.7	1802.4	1534.6	1009.2	1955.5	1826.9	1545	1042.8
Time (UTC)	18:11	18:11	18:11	18:36	18:36	18:36	17:56	17:56	17:56	17:56
Solar distance (AU)	1.0160	1.0160	1.0160	1.0004	1.0004	1.0004	1.0004	1.0004	1.0004	1.0004
Solar zenith angle (°)	56.5	56.5	56.5	55.4	55.4	55.4	57.3	57.3	57.3	57.3
Solar azimuth angle (°)	160.5	160.5	160.5	168.09	168.09	168.09	156.3	156.3	156.3	156.3
View zenith angle (°)	35.5	35.5	35.5	3.31	3.31	3.31	1.8	1.8	1.8	1.8
View azimuth angle (°)	100.5	100.5	100.5	283.7	283.7	283.7	102.9	102.9	102.9	102.9
Rayleigh optical depth	0.1752	0.0398	0.0157	0.0927	0.0455	0.0166	0.1517	0.0790	0.0430	0.0168
Aerosol optical depth	0.0610	0.0404	0.0302	0.5020	0.0411	0.0300	0.0575	0.0481	0.0404	0.0300
BRF factor for satellite sensor case	1.45	1.45	1.45	1	1	1	1	1	1	1
Test site %RHO from QUASAR (TQ)	5.3	9.9	16.7	7.7	9.6	16.8	6.2	8.1	9.8	16.8
Val site %RHO from GER (G)	6.2	10.5	18.4	8.3	10.3	18.5	6.8	8.8	10.4	18.5
ΔRHO=%(TQ−G)/G	−14.9%	−5.9%	−9.0%	−7.6%	−6.7%	−9.1%	−9.2%	−7.6%	−6.2%	−9.1%
Val site %RHO from QUASAR (VQ)	5.5	10.3	18.1	8.1	10.0	18.2	6.5	8.6	10.1	18.2
ΔRHO=%(VQ−G)/G	−10.7%	−2.1%	−1.4%	−2.3%	−2.9%	−1.6%	−4.6%	−2.5%	−2.6%	−1.6%
Average image DSL for test site				36.03	35.42	41.83	68.12	27.80	40.92	39.98
Nominal post-launch cal gain				0.859	1.008	1.178	1.6599	0.8510	1.2411	1.2277
Nominal post-launch cal offset				0	0	0	2.523	2.417	1.452	1.854
TOA L^* from nominal PLC (N)	58.6	37.6	36.5	41.9	35.1	35.5	39.5	29.8	31.8	31.1
TOA L^* from QUASAR PLC (Q)	50.9	45.8	45.4	37.4	33.0	32.5	40.2	34.5	31.6	31.1
Δ TOA L^*=%(Q−N)/N	−13.2%	21.9%	24.3%	−10.9%	−6.2%	−8.6%	1.7%	15.8%	−0.5%	0.1%

[a] UTC=coordinated universal time; AU=astronomical units; RHO=surface reflectance;
DSL=digital signal level; PLC=post-launch calibration; TOA=top of atmosphere.
DSL units are image counts; radiances L^* units are W/(m^2 sr μm); irradiances units are W/(m^2 μm); gain units are counts/radiance.
SPOT-4 VGT image data were provided in calibrated units, not DSL.
Newell County test site latitude=50°18′20″; longitude=−111°37′32″; elevation=750 m.
Atmospheric parameters: ozone content (cm atm)=0.319; water vapour content (g/cm^2)=1.35; AOD550=0.05.

Table 6
Average excursions of QUASAR TOA radiances from nominal values: averaged over the number of spectral band cases (left-hand side); weighted over the number of satellite sensor cases (right-hand side)

| Satellite sensor | Weighted by the number of spectral band cases | | | | | | Weighted by the number of satellite sensor cases | | | | | |
| | RVPN | | NCRA | | Both sites | | RVPN | | NCRA | | Both sites | |
	Average TOA radiance excursion (%)	Number of spectral band cases	Average TOA radiance excursion (%)	Number of spectral band cases	Average TOA radiance excursion (%)	Number of spectral band cases	Average TOA radiance excursion (%)	Number of satellite sensor cases	Average TOA radiance excursion (%)	Number of satellite sensor cases	Average TOA radiance excursion (%)	Number of satellite sensor cases
Airborne data acquisition days												
AVHRR	7.3	1	13.0	2	11.1	3	7.3	1	13.0	2	11.1	3
VGT	4.1	3	19.8	3	12.0	6	4.1	1	19.8	1	12.0	2
TM			4.5	4	4.5	4			4.5	1	4.5	1
HRV			8.5	3	8.5	3			8.5	1	8.5	1
SeaWiFS	3.1	8	6.3	16	5.2	24	3.1	1	6.3	2	5.2	3
Overall	3.7	12	8.2	28	6.9	40	4.85	3	10.2	7	8.6	10
Other days												
AVHRR	6.9	8	7.8	5	7.3	13	6.9	8	7.8	5	7.3	13
VGT			9.5	3	9.5	3			9.5	1	9.5	1
TM	24.8	4	5.1	4	14.9	8	24.8	1	5.1	1	14.9	2
HRV	14.9	3	3.8	3	9.3	6	14.9	1	3.8	1	9.3	2
SeaWiFS	16.0	8	11.8	48	12.4	56	16.0	1	11.8	6	12.4	7
Overall	14.2	23	10.6	63	11.6	86	15.6	11	9.2	14	12.0	25
All days												
AVHRR	7.0	9	9.3	7	8.0	16	7.0	9	9.3	7	8.0	16
VGT	4.1	3	14.7	6	11.1	9	4.1	1	14.7	2	11.1	3
TM	24.8	4	4.8	8	11.5	12	24.8	1	4.8	2	11.5	3
HRV	14.9	3	6.2	6	9.1	9	14.9	1	6.2	2	9.1	3
SeaWiFS	9.5	16	10.4	64	10.3	80	9.5	2	10.4	8	10.3	10
Overall	10.6	35	9.9	91	10.1	126	12.0	14	9.5	21	10.5	35

An excursion is defined as the absolute value of the relative difference between QUASAR and nominal TOA radiances.

surface reflectance retrieval using the Modtran-3 radiative transfer code and a look-up table approach (Staenz & Williams, 1997). The main inputs to this procedure are atmospheric aerosol optical depth at 0.550 μm (AOD550), terrain elevation, aircraft altitude, and solar zenith angle pertinent to the given flight line. Desert and continental aerosol models were assumed for the RVPN and NCRA test sites, respectively. The atmospheric ozone content is the standard value for a US62 (at RVPN) or a mid-latitude summer (at NCRA) atmospheric model, taking the terrain elevation and sensor altitude into account. The atmospheric water vapour content (UH_2O) is considered to be a free parameter that is determined as part of an ISDAS optimization scheme (Staenz & Williams, 1997). The resulting values of UH_2O were 1.10 g/cm^2 for the RVPN test site, and 2.20 g/cm^2 (August) and 1.35 g/cm^2 (October) for the NCRA test site. ISDAS also takes into account the scan-angle geometry for the *casi* sensor, adjusted for the reduced scan-angle range resulting from the aforementioned test site segment extraction. The atmospheric correction step for both *casi* and AVIRIS data can be represented by the operation (Eq. (2)):

$$\overline{\rho}_{ikl}(\theta_{s,l}, \theta_v, \Delta\phi_l) = f^{-1}\{\overline{L^*_{ikl}}(\theta_{s,l}, \theta_v, \Delta\phi_l)\}, \qquad (2)$$

where $\overline{\rho}$ = surface reflectance averaged over image lines. The atmospheric correction is expressed in this way because apparent at-sensor radiance is not a linear function of surface reflectance (cf. Tanre et al., 1990, for example).

The surface reflectance data set is still a function of the surface's bidirectional reflectance characteristics at this point in the data processing sequence. Therefore, the surface reflectances should, in principle, be adjusted to a standard geometry such as nadir view angle and the average solar zenith angle $\overline{\theta}_s$ during the airborne data acquisition (Eq. (3)):

$$\overline{\rho}_{ikl}(\overline{\theta}_s, 0°, 0°) = \overline{\rho}_{ikl}(\theta_{s,l}, \theta_v, \Delta\phi_l)\left[\frac{\overline{\rho}(\overline{\theta}_s, 0°, 0°)}{\overline{\rho}(\theta_{s,l}, \theta_v, \Delta\phi_l)}\right]_{\text{BRF}}, \qquad (3)$$

where BRF is used to denote a bidirectional reflectance factor adjustment or model. In practice, the ground-based acquisition of off-nadir spectral reflectance data at the two test sites has been limited to date and bidirectional reflectance factor characterizations for general use have yet to be fully developed for the playa and rangeland surfaces. Approximate BRF adjustments are attempted at a later step in the processing when taking specific satellite observation geometries into account. However, for the
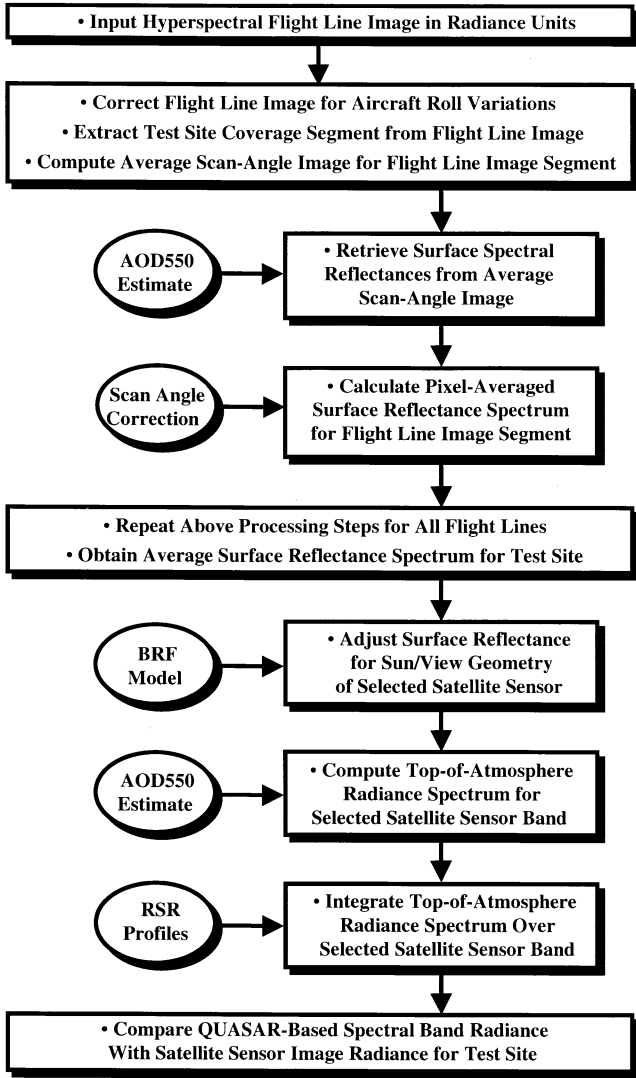
• Input Hyperspectral Flight Line Image in Radiance Units

• Correct Flight Line Image for Aircraft Roll Variations
• Extract Test Site Coverage Segment from Flight Line Image
• Compute Average Scan-Angle Image for Flight Line Image Segment

AOD550 Estimate → **• Retrieve Surface Spectral Reflectances from Average Scan-Angle Image**

Scan Angle Correction → **• Calculate Pixel-Averaged Surface Reflectance Spectrum for Flight Line Image Segment**

• Repeat Above Processing Steps for All Flight Lines
• Obtain Average Surface Reflectance Spectrum for Test Site

BRF Model → **• Adjust Surface Reflectance for Sun/View Geometry of Selected Satellite Sensor**

AOD550 Estimate → **• Compute Top-of-Atmosphere Radiance Spectrum for Selected Satellite Sensor Band**

RSR Profiles → **• Integrate Top-of-Atmosphere Radiance Spectrum Over Selected Satellite Sensor Band**

• Compare QUASAR-Based Spectral Band Radiance With Satellite Sensor Image Radiance for Test Site

Fig. 6. Detailed data flow scheme for the QUASAR monitoring method. AOD550 = aerosol optical depth at 0.550 μm; BRF = bidirectional reflectance factor; and RSR = relative spectral response.

purpose of normalizing the *casi* airborne data to nadir and to an average sun angle for the data acquisition period (approximately 1.5 h), an empirical scan-angle profile correction is used. This correction is not applied to AVIRIS imagery given the limited scan-angle range and single flight line.

The 212 pixels of the *casi*-based surface reflectance view-angle image are then averaged to form a final average surface reflectance spectrum for the portion of the test site covered by the given flight line (Eq. (4)):

$$\overline{\rho}_{kl}(\overline{\theta}_s, 0°, 0°) = \frac{1}{I} \sum_{i=1}^{I} \overline{\rho}_{ikl}(\overline{\theta}_s, 0°, 0°), \tag{4}$$

where I = total number of pixels in a given scan line. All of the preceding processing steps are repeated for all *casi* flight

lines to yield an average surface reflectance spectrum for the entire test site:

$$\overline{\rho}_k(\overline{\theta}_s, 0°, 0°) = \frac{1}{L} \sum_{l=1}^{L} \overline{\rho}_{kl}(\overline{\theta}_s, 0°, 0°), \tag{5}$$

where L = total number of flight line segments.

In addition to the average surface reflectance spectrum, standard deviation reflectance spectra are also calculated to serve as one measure of overall test site variability. Spatial uniformity studies are also being pursued in parallel to the work described in this paper. In time, an improved understanding of each test site should make it possible to clarify whether satellite image pixels can be extracted from anywhere in a given test site or whether some parts of the site differ significantly from the average and should be avoided in the analysis. Another concern is the potential impact of any data gap or redundancy in *casi* test site coverage resulting from aircraft attitude variations and the test site extraction procedure. Given the relatively uniform land cover at the selected test sites, this problem will not likely be a large source of error, but it has yet to be addressed. For now, it is assumed that the average surface reflectance spectrum resulting from the processing scheme just described is representative of the entire 7×7 km^2 test site.

4.2. Top-of-atmosphere radiance predictions

The data processing to this point has yielded an estimate of the average surface spectral reflectance for the test site (Eq. (5)), as retrieved from the hyperspectral airborne imagery. Moreover, the average surface reflectance spectrum is standardized to nadir view angle and average solar zenith angle. The result constitutes a ground reference data set that can be used to monitor any appropriate satellite sensor observing the test site on the same day or within a few days if conditions have not changed significantly. In particular, there is the potential to estimate the apparent radiance that these satellite sensors should see at the TOA. There are three main steps involved in generating the TOA radiance predictions: a BRF adjustment of the surface reflectance spectrum to the geometries pertinent to the satellite observation of interest, an atmospheric computation to convert the surface spectral reflectance to TOA spectral radiance, and a sensor spectral band integration.

The BRF adjustment step can be represented by the operation (Eq. (6)):

$$\overline{\rho}_k(\theta_{s,sat}, \theta_{v,sat}, \Delta\phi_{sat})$$
$$= \overline{\rho}_k(\overline{\theta}_s, 0°, 0°) \left[\frac{\overline{\rho}(\theta_{s,sat}, \theta_{v,sat}, \Delta\phi_{sat})}{\overline{\rho}(\overline{\theta}_s, 0°, 0°)} \right]_{BRF}, \tag{6}$$

where the "sat" subscript indicates angles pertinent to the solar illumination and satellite view geometry when imaging

the test site. BRF adjustment factors for QUASAR processing for the RVPN test site are based on surface measurements using a BRF camera apparatus (Nandy, Thome, & Biggar, 1998; Nandy, Thome, & Biggar, 1999) and for the NCRA test site on the Chen-modified Roujean model for barren land (Chen & Cihlar, 1997; Roujean, Leroy, & Deschamps, 1992). The use of model results for NCRA BRF adjustments is clearly a significant potential source of error. Moreover, for each satellite sensor case, a single BRF adjustment factor is used regardless of wavelength, although it is well known that the spectral dependence of BRF effects is of second order.

The atmospheric computation to estimate TOA radiance is carried out separately for each satellite observation case and each spectral sensor band and is denoted as:

$$\overline{L_k^*}(\theta_{s,sat}, \theta_{v,sat}, \Delta\phi_{sat}) = f\{\overline{\rho}_k(\theta_{s,sat}, \theta_{v,sat}, \Delta\phi_{sat})\}, \qquad (7)$$

where the atmospheric parameters are assumed to be the same as for the surface reflectance retrieval from the airborne imagery, while allowing for sensor altitude differences.

In all cases, the atmospheric parameters for a given site pertain to those that were estimated on the airborne data acquisition date and they are assumed to remain unchanged for the other days examined for the feasibility of temporal extensions. The Newell County test site is located in eastern Alberta, well away from the mountains and benefits from some of the clearest and driest atmospheric conditions on the continent on average. Although its vicinity is more mountainous, the Railroad Valley test site benefits from the playa's high altitude, above-average albedo, and large spatial extent, as well as from the tendency for clouds to stay along mountain ridges in that region. In any event, errors in atmospheric characterization and radiative transfer code calculations are not expected to change the QUASAR results significantly. Tests show that, if the unknown aerosol optical depth on the satellite overpass day was actually double the amount measured on the *casi* flight day and assumed for the QUASAR analysis, the predicted TOA radiance in TM band 1 as an example would increase by 0.5%. This low sensitivity is an advantageous feature of in-flight cross-calibrations between sensors. It is due to the two-way use of the same estimate for aerosol optical depth in both the *casi*-based surface reflectance retrieval and the subsequent satellite sensor TOA radiance prediction. It should also be mentioned that surface BRF effects are not included in the atmospheric computations, but they are expected to be included in future versions of ISDAS. Based on the results of Santer, Schmehtig, and Thome (1996) for the White Sands test site, the inclusion of BRF effects and proper adjacency effects as appropriate in the radiative transfer code calculations will alter TOA radiances by a few percent at most.

The wavelength coverage of the test site by the hyperspectral airborne sensor will dictate which satellite sensor spectral bands can be considered. The relative spectral response profile $S(\lambda)$ for each spectral band is convolved with the TOA radiance spectrum from Eq. (7) to generate an apparent radiance in that spectral band (Eq. (8)):

$$\overline{L_{band}^*}(\theta_{s,sat}, \theta_{v,sat}, \Delta\phi_{sat})$$
$$= \int_{\lambda min}^{\lambda max} \overline{L_k^*}(\theta_{s,sat}, \theta_{v,sat}, \Delta\phi_{sat})S(\lambda)d\lambda, \qquad (8)$$

where λ_{min} and λ_{max} are the wavelength limits of the spectral band's response profile.

4.3. Satellite sensor calibration predictions

It is assumed that the TOA radiance estimates obtained from the QUASAR methodology (i.e., the output of the last step in the data flow diagram in Fig. 6) for the various satellite sensor spectral bands are representative of the entire 7×7 km^2 test site. With a reference area of that size, it is possible to accommodate several image pixels even for large footprint sensors and still stay well within the boundaries of the area to allow for location errors.

For comparison, the "nominal" post-launch calibration coefficients are obtained from the pertinent sources. For AVHRR, the coefficients were obtained from NASA's Goddard Space Flight Center and based on ocean and cloud scene methodologies (Vermote & Kaufman, 1998). For SeaWiFS, the calibration was obtained by running the SeaWiFS Data Analysis System (SeaDAS) package (Fu, Baith, & McClain, 1998). For TM, HRV, and VGT, the nominal calibration coefficients were taken from the product tape header and documentation. The TOA radiances in each spectral band are calculated from these nominal post-launch calibration coefficients using the average digital signal levels (DSL in counts) from the image of each test site and the equation (Eq. (9)):

$$L_{band}^* = (\overline{DSL}_{band} - offset_{band})/gain_{band}. \qquad (9)$$

The main QUASAR monitoring results are then comparisons between TOA radiances obtained from the QUASAR monitoring approach and those based on nominal post-launch calibration coefficients.

5. Uncertainty estimates

According to Biggar, Slater, and Gellman (1994), the radiance-based and reflectance-based approaches to vicarious calibration have uncertainties of 3–5% (1σ), respectively, for TOA radiance predictions in the visible spectral region under good conditions at the White Sands test site. The error estimate for the reflectance-based method takes

into account uncertainties in atmospheric characterization, surface characterization, and radiative transfer code calculations, added together in a root-sum-square fashion. Planned improvements in these characterizations and calculations by the University of Arizona are expected to reduce the uncertainty from 5% to 3.5%. Radiance-based calibration involves fewer steps and the uncertainty depends primarily on the calibration and deployment of the reference radiometer. For cross-calibrations between a sensor such as NOAA AVHRR and a reference sensor such as SPOT HRV using the Railroad Valley playa, it has been estimated that the uncertainty is ±6% (1σ) or ±5% with planned improvements (Scott, Thome, & Brownlee, 1996). This error estimate is based on the root sum squares of errors from four sources: the reference sensor calibration (4.9%; (Biggar et al., 1994)), image registration (2.5%), spectral correction (2.0%), and reflectance anisotropy correction (1.7%). An error budget model is under development for the QUASAR monitoring approach (Bergeron, O'Neill, Royer, & Teillet, 1998). For now, the uncertainty in the QUASAR method is assumed to be approximately 6% since it is essentially an image-based cross-calibration approach.

6. Methodology validation results

For the data acquisition campaign at the RVPN test site, independent data acquisition by the airborne hyperspectral AVIRIS, the ground-based FieldSpec spectrometer, and the Reagan solar radiometer provided an opportunity to perform an initial validation of key elements of the QUASAR methodology.

6.1. Sunphotometer measurements

As already mentioned, AOD550 values retrieved from the Microtops-II and Reagan sunphotometer measurements at the RVPN test site typically agreed to within 0.01 and did not differ by more than 0.03 over the course of several days of observations. This represents reasonable agreement between sunphotometers.

6.2. Surface spectral reflectance

Fig. 7 shows a comparison of surface reflectance spectra averaged over the 100×100 m^2 validation site and, in the case of the FieldSpec spectrometer, a nearby area at the RVPN test site. The four curves correspond to ground-based GER3700 and FieldSpec measurements, and atmospherically corrected *casi* and AVIRIS image data. The *casi*-based and AVIRIS-based surface reflectance spectra correspond to the half-way point in the processing data flow shown in Fig. 6. The *casi* spectrum clearly differs from that obtained from the AVIRIS data as well as from both of the ground-based spectrometers. The discrepancy is likely due to calibration uncertainties in the *casi*
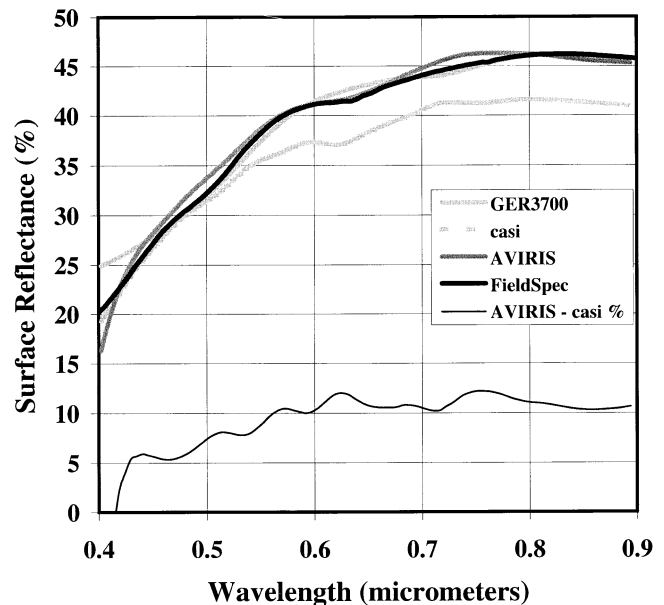
Fig. 7. Percent surface spectral reflectance comparisons for the RVPN validation site. The lowest curve is the percentage relative difference between the AVIRIS and *casi* reflectance.

data. The percent relative differences between the AVIRIS and the *casi* spectra are also plotted, indicating a discrepancy ranging from roughly 5% in the blue to approximately 10% in the red and near-infrared.

6.3. Band-integrated surface reflectances

Fig. 8 shows the aforementioned surface spectral reflectances integrated over 19 satellite sensor spectral bands, namely, sensor (spectral bands): AVHRR (1), SPOT-4 VGT (1−3), OrbView-2 SeaWiFS (1−8), Landsat TM (1−4), and SPOT-1/2 HRV (1−3). The GER3700, AVIRIS-based, and *casi*-based surface reflectances in these satellite sensor spectral bands are plotted against the FieldSpec reflectances for the RVPN validation site. The ±2% error bars represent the standard deviations of the measurement sets only and not measurement uncertainties. The agreement is generally within ±2% except for the *casi*-based points and the bluest spectral band cases, which include SeaWiFS spectral bands 1−4 and TM spectral band 1. The worst case at the lower end of the graph in Fig. 8 is SeaWiFS spectral band 1, which has a central wavelength of 0.412 μm. The wavelength ranges of the airborne and surface sensors do not adequately encompass the shorter wavelength portions of the bluest satellite spectral bands under investigation. Nevertheless, the results shown in Fig. 8 are reasonable given the completely independent data, methods, and spatial scales involved. As a function of FieldSpec surface reflectances, the slope and intercept of the GER3700 surface reflectances are 0.932% and 2.86%, respectively, and the correlation between the GER3700 and FieldSpec reflectances has a coefficient of determination (r^2) of .986. The (slope, inter-
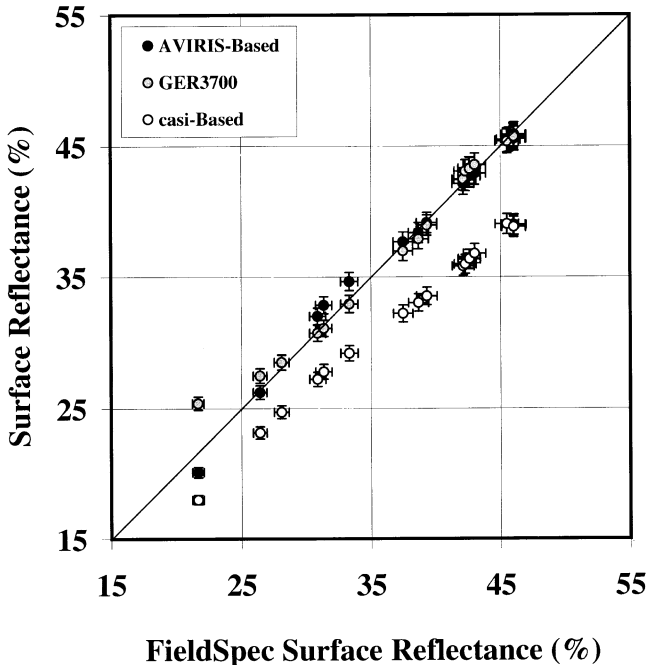
Fig. 8. Percent surface reflectance comparisons in selected satellite sensor bands for the RVPN validation site. The $\pm 2\%$ error bars represent standard deviations typical of the data sets. The diagonal line is the unity slope line.

cept) of the AVIRIS-based and *casi*-based surface reflectances are (0.984, 0.638) and (0.821, 1.39), respectively, and the correlations between these reflectances and FieldSpec reflectances are $r^2=.992$ and .996, respectively.

6.4. Calibration correction for casi-based results

The methodology validation results clearly indicate a discrepancy in the *casi* calibration and, therefore, a correction is needed in order to use the *casi*-based results generated for the two NCRA campaigns. Since the AVIRIS is known to be a well-calibrated sensor and the same *casi* sensor was used in all three 1998 campaigns, the ratio spectrum shown in Fig. 9 was used to correct the average *casi*-based surface reflectances obtained for the NCRA test site.

6.5. Spatial and temporal consistency of airborne hyperspectral imagery

For both the RVPN and NCRA test sites, the average surface reflectance spectrum retrieved from corrected *casi* data for the whole test site (not shown) compared favourably with the average GER spectrum acquired for the ground validation site, as well as with the average *casi* spectrum for the flight line segment that included the validation site. A partial set of clear-sky *casi* data were acquired at RVPN on June 16, 1998, but they have not been used in the QUASAR analyses. A comparison with the *casi* data from June 17 indicates that *casi* radiances obtained on two consecutive days over the main part of the RVPN test
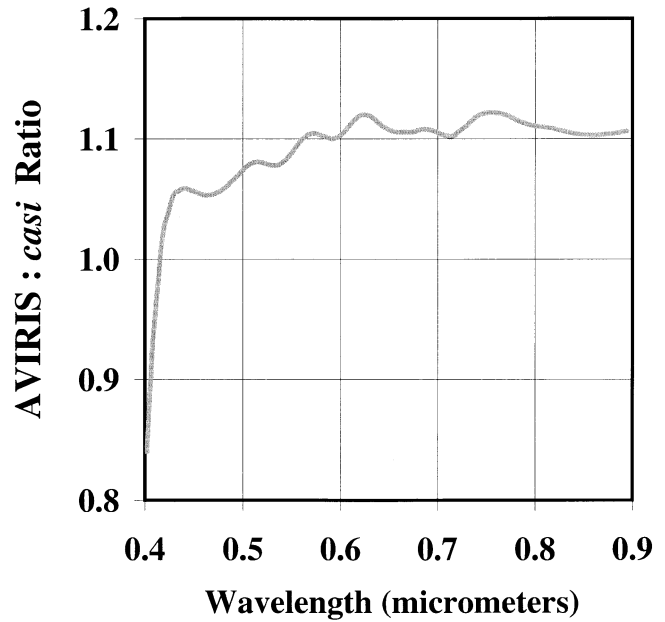
Fig. 9. Ratio comparison of the surface reflectance spectra retrieved from the airborne AVIRIS and *casi* image data for the RVPN validation site.

site (not shown) are essentially identical across the spectrum, thus providing an indication of the day-to-day repeatability of the airborne hyperspectral data acquisition and the short-term temporal stability of the playa surface.
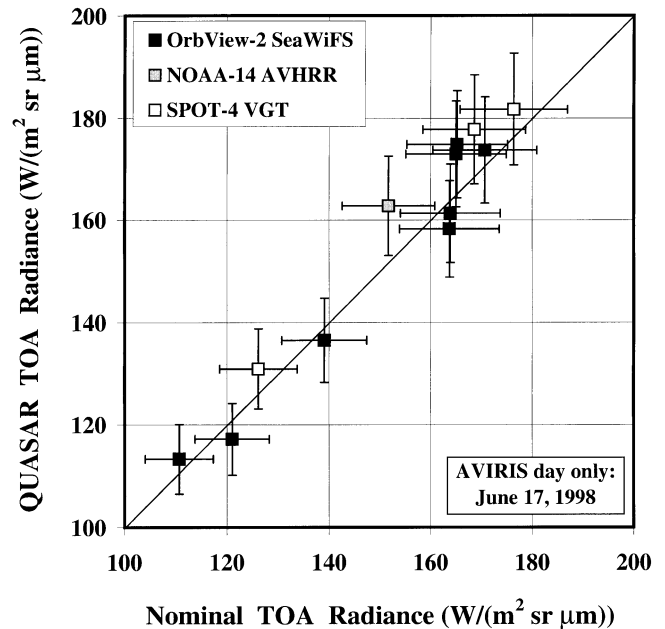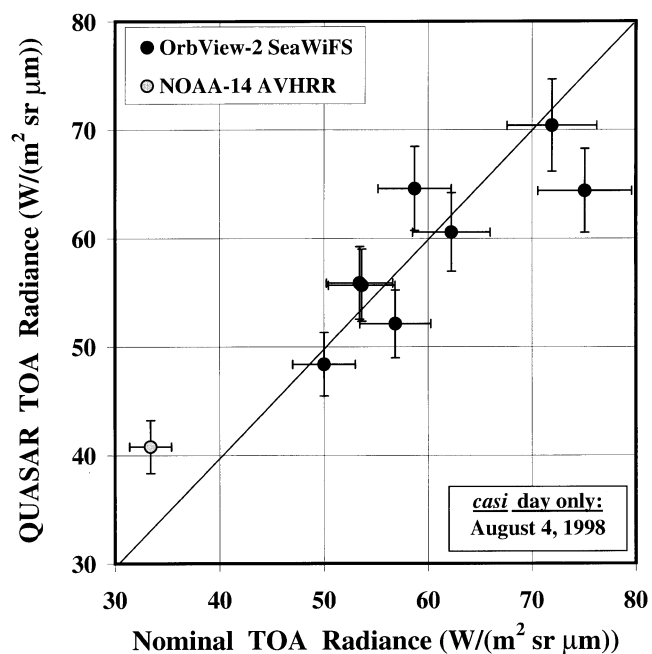

Fig. 10. Comparison of QUASAR-based and nominal TOA radiances for the RVPN test site for June 17, 1998. The satellite sensor cases include NOAA-14 AVHRR spectral band 1, SPOT-4 VGT spectral bands 1–3, and OrbView-2 SeaWiFS spectral bands 1–8. The error bars represent $\pm 6\%$ uncertainty levels. The diagonal line is the unity slope line. The linear fit of the radiance data points is $y = 1.076x - 8.22$, and $r^2=.949$.

7. QUASAR monitoring results for satellite sensors

The main QUASAR results for each test site consist of AVIRIS-based or *casi*-based TOA radiance estimates and their percentage differences with respect to satellite image-based TOA radiances determined independently using nominal post-launch calibration coefficients. The differences are defined as (QUASAR − nominal)/nominal in percent. This comparison corresponds to the final step in the processing data flow shown in Fig. 6.

7.1. Results for the RVPN test site (June 17)

AVIRIS-based TOA radiance estimates were generated for NOAA-14 AVHRR spectral band 1, SPOT-4 VGT spectral bands 1−3, and OrbView-2 SeaWiFS spectral bands 1−8, which imaged the test site on the day of the airborne data acquisitions (June 17). The results are shown in Fig. 10 and Table 3, which includes the main observational parameters for the satellite sensor acquisitions. For 12 spectral bands from the three sensors, the QUASAR monitoring approach predicts TOA radiances that differ from the nominal TOA radiances by − 3.3% to + 7.3% (relative). The error bars in Fig. 10 represent ± 6% uncertainty levels. For the QUASAR result axis, this corresponds to the error estimate of Scott et al. (1996) for cross-calibration using the Railroad Valley playa. For the nominal calibration result axis, although the various satellite sensors
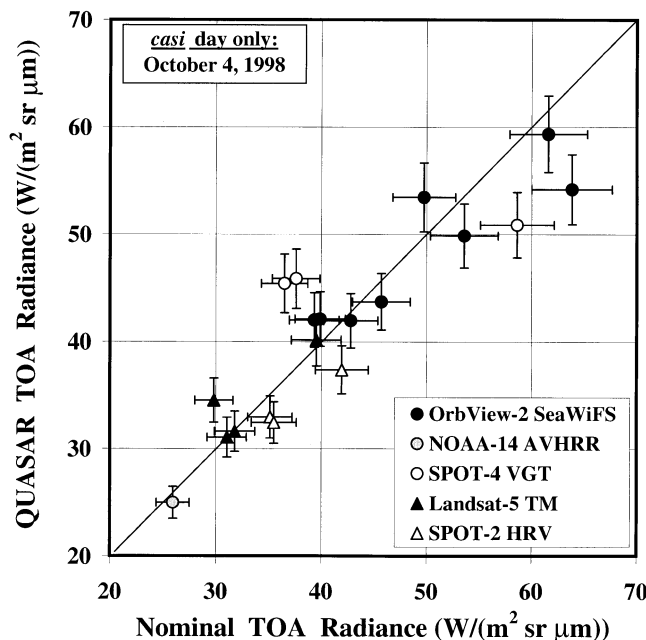
Fig. 12. Comparison of QUASAR and nominal top-of-TOA radiances for the NCRA test site for October 4, 1998. The satellite sensor cases include NOAA-14 AVHRR spectral band 1, SPOT-4 VGT spectral bands 1−3, OrbView-2 SeaWiFS spectral bands 1−8, Landsat-5 TM spectral bands 1−4, and SPOT-2 HRV spectral bands 1−3. The error bars represent ± 6% uncertainty levels. The diagonal line is the unity slope line. The linear fit of the radiance data points is $y = 0.761x + 9.74$, and $r^2 = .813$.

involved have different calibration uncertainties, ± 6% has been used as a representative value. The slope and intercept of the 12 radiance data points in Fig. 10 are 1.076 and − 8.22, and $r^2 = .949$.

7.2. Results for the NCRA test site (August 4)

Based on the data acquisition campaign at the NCRA test site on August 4, 1998, *casi*-based QUASAR monitoring results were obtained for NOAA-14 AVHRR spectral band 1 and OrbView-2 SeaWiFS spectral bands 1−8. Data processing and calibration corrections were as described previously. Fig. 11 and Table 4 indicate that the QUASAR results for SeaWiFS are within 10% of nominal values except for spectral band 1, whereas the AVHRR result is well above nominal (+22% relative). Specific reasons for the AVHRR mismatch are not yet understood, but the most likely cause is thought to be an inadequate BRF adjustment. The slope and intercept of the nine radiance data points in Fig. 11 are 0.675 and 18.3, and $r^2 = .826$.

7.3. Results for the NCRA test site (October 4)

Results for October 4 are shown in Fig. 12 and Table 5. Five satellite sensors imaged the test site on that day. The *casi*-based QUASAR monitoring results were generated for NOAA-14 AVHRR spectral band 1, OrbView-2 SeaWiFS spectral bands 1−8, SPOT-4 VGT spectral bands 1−3,

Fig. 11. Comparison of QUASAR and nominal TOA radiances for the NCRA test site for August 4, 1998. The satellite sensor cases include NOAA-14 AVHRR spectral band 1 and OrbView-2 SeaWiFS spectral bands 1−8. The error bars represent ± 6% uncertainty levels. The diagonal line is the unity slope line. The linear fit of the radiance data points is $y = 0.675x + 18.3$, and $r^2 = .826$.

Landsat-5 TM spectral bands 1–4, and SPOT-2 HRV spectral bands 1–3. As indicated in Fig. 12 and Table 5, the QUASAR results for SeaWiFS are within 7.5% of nominal values except for spectral band 1, whereas the AVHRR result is close to the nominal value (-3.7% relative). Reasons for the larger mismatches for the VGT results (Table 5) are not yet understood. Results for TM are within a few percent of the nominal values, except for spectral band 2, and HRV results are within 11% of the nominal values. The slope and intercept of the 19 radiance data points in Fig. 12 are 0.761 and 9.74, and $r^2=.813$. If the 28 radiance data points in Figs. 11 and 12 are combined, the linear fit of the TOA radiance points is $y = 0.810x + 8.61$, and $r^2=.867$.

7.4. Discussion of QUASAR monitoring results

Figs. 13 and 14 summarize the QUASAR monitoring results obtained for the airborne data acquisition days at the two test sites. Five satellite sensors encompassing a total of 40 spectral band cases are included (Tables 3–5). The linear fit of the comparison between QUASAR-based and nominal TOA radiances is $y = 1.026x - 1.26$, and $r^2=.990$. Thus, while problems arise in certain cases and

the results for the NCRA test site show greater scatter, there is good correspondence overall between QUASAR-based and nominal radiometric calibration results. The use of the lower-radiance rangeland test site is beneficial in that the combined data set yields a better radiance correlation than do the individual test sites treated separately. Fig. 14 plots the percent relative difference between the QUASAR-based and nominal calibrations as a function of the nominal TOA radiance values. Greater differences for the lower-radiance NCRA test site than for the RVPN test site are consistent with a roughly constant error in absolute radiance terms.

The main error source contributing to the scatter in the QUASAR results is considered to be attributable to inadequate BRF adjustments. Confirmation that this is the main error source will require further study. It should be mentioned that the October NCRA data set is particularly challenging in this respect since the solar zenith angles are in the $55-60°$ range. There are also uncertainties in the nominal calibrations, but their discussion is beyond the scope of this paper.

The 40 spectral band cases that make up the current QUASAR monitoring results have been examined as a function of five observational parameters listed in Tables

Airborne data acquisition days only:
RVPN (AVIRIS): June 17, 1998
NCRA (*casi*): August 4, 1998
NCRA (*casi*): October 4, 1998

- ● **OrbView-2 SeaWiFS - NCRA**
- ■ **OrbView-2 SeaWiFS - RVPN**
- ○ **NOAA-14 AVHRR - NCRA**
- □ **NOAA-14 AVHRR - RVPN**
- ○ **SPOT-4 VGT - NCRA**
- □ **SPOT-4 VGT -RVPN**
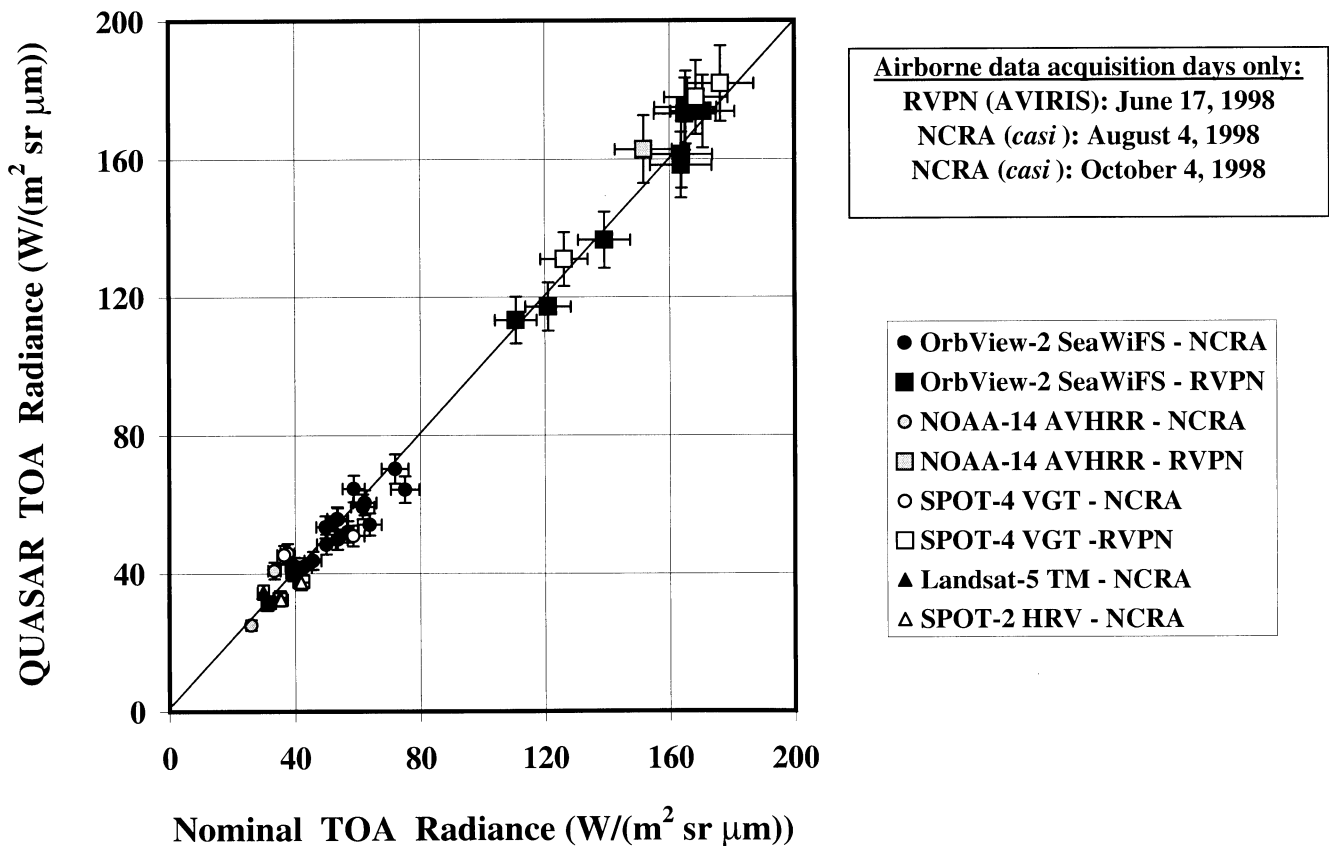- ▲ **Landsat-5 TM - NCRA**
- △ **SPOT-2 HRV - NCRA**

Fig. 13. Comparison of QUASAR-based and nominal TOA radiances for the three airborne data acquisition days (one at the RVPN test site and two at the NCRA test site). The satellite sensor cases include all of the cases shown in Figs. 10–12. The error bars represent ±6% uncertainty levels. The diagonal line is the unity slope line. The linear fit of the radiance data points is $y = 1.026x - 1.26$, and $r^2=.990$.
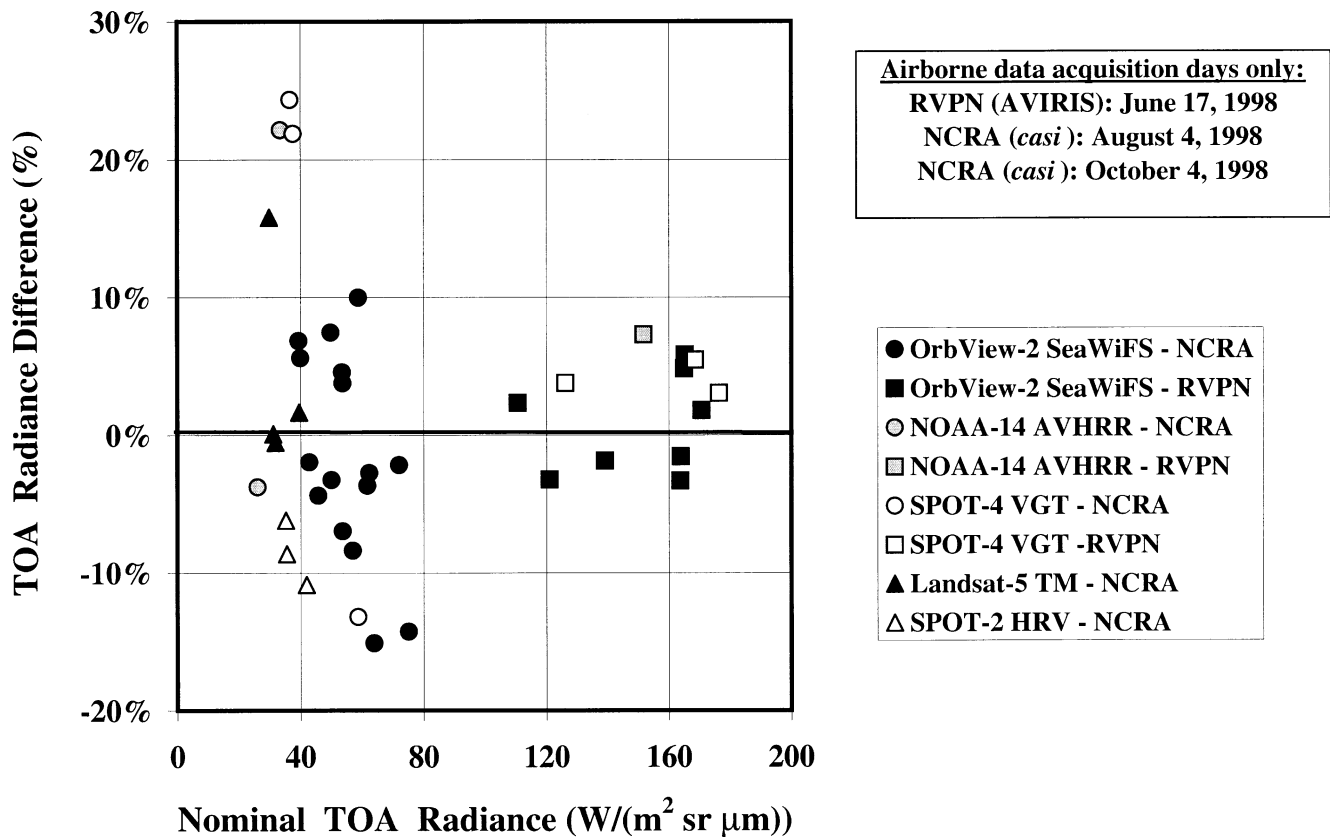
Fig. 14. Percent relative difference between the QUASAR and nominal TOA radiances as a function of the nominal values based on the three data acquisition campaigns (one at the RVPN test site and two at the NCRA test site). The satellite sensor cases are the same as for Fig. 13.

3–5, i.e., ΔTOAL^* was plotted (not shown), in turn, as a function of central wavelength, solar zenith angle, satellite zenith angle, relative azimuth, and BRF adjustment factor. No significant trends were found. On the basis of the 40 cases examined, it is tentatively concluded that the QUASAR approach is not sensitive in any systematic way to any of these observational parameters.

8. Temporal extensions to other days

The availability of satellite imagery within a few days of the airborne data acquisition days made it possible to consider temporal extensions of the QUASAR monitoring results. In these cases, the atmospheric parameters used in the processing pertain to those that were estimated on the airborne data acquisition day and they are assumed to remain unchanged for the other days. The test site surface is also assumed to have remained unchanged. Clearly, these assumptions are potential sources of error in extending results temporally and, in due course, the trade-off between more data points and reduced accuracy will have to be examined. On the other hand, in the QUASAR processing, actual illumination and viewing geometries pertinent to each satellite sensor image acquisition were used and an appropriate BRF adjustment factor was computed and used accordingly.

8.1. Results for the RVPN test site (June)

QUASAR TOA radiance estimates for AVHRR cases on other dates around the airborne data acquisition day (June 18–22) differ increasingly from the June 17 result as a function of temporal extension. TOA radiance differences as previously defined change systematically from +7.3% on June 17 to −13.0% on June 22 (Fig. 15, which shows temporal trends for red spectral bands only in order to facilitate intercomparisons). Such a trend is consistent with an increase in surface reflectance with a drying playa over time and/or increasingly hazier atmospheric conditions over time. Increased surface reflectance and/or increased atmospheric contribution in visible spectral bands would lead to higher nominal TOA radiances compared to the QUASAR values obtained on the airborne data acquisition day. Contrary to this trend, for unknown reasons, results for the eight SeaWiFS spectral bands for June 18 (not shown) differ from nominal values by an average of +16%.

With respect to small footprint sensors TM and HRV, neither of the satellite sensor data sets was acquired on the same day as the airborne hyperspectral data acquisition. Therefore, the generation of QUASAR monitoring results in these cases relies exclusively on temporal extrapolations of surface and atmospheric conditions ranging from 1 to 3
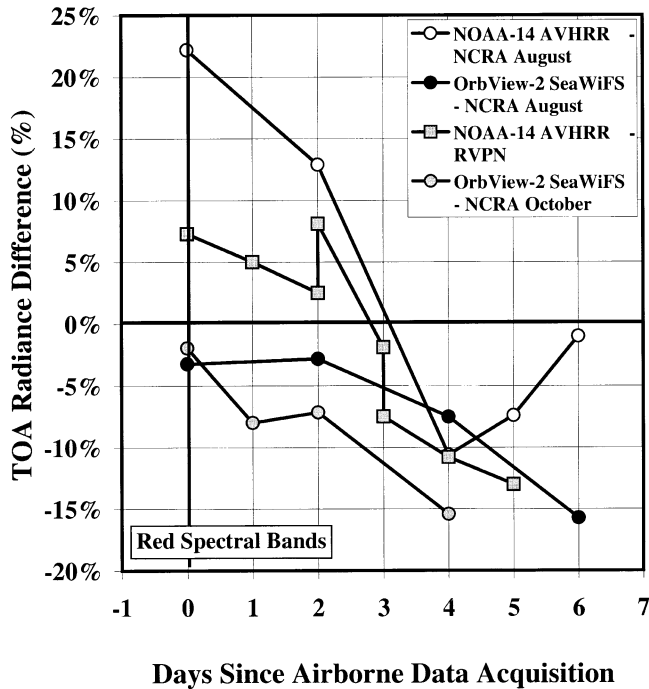
Fig. 15. Percent relative difference between the QUASAR and nominal TOA radiances as a function of temporal extension in days since airborne data acquisition. Only red spectral bands (i.e., near 0.65 μm) are included. Points are connected as a visual aid only. Day 0 is the day of the airborne data acquisition for each of the three test site campaigns.

days. Results for the four TM spectral bands for June 14 differ from nominal values by an average of +23%. Results for the three SPOT-1 HRV spectral bands for June 18 differ from nominal values by an average of −15%. Thus, the RVPN QUASAR data sets do not provide a good reference for Landsat-5 TM 3 days earlier (June 14) and SPOT-1 HRV a day later (June 18). This situation is likely to be due, at least in part, to significant changes in the playa surface while it was drying after a rainy period earlier in the month. The days following a wet period should be avoided and/or a better knowledge of the characteristics of the RVPN test site as a function of time needs to be developed.

8.2. Results for the NCRA test site (August)

QUASAR TOA radiances estimates for SeaWiFS cases on other dates around the airborne data acquisition day (August 6–10) also differ increasingly from the August 4 results as a function of temporal extension. Fig. 15 shows this trend for SeaWiFS band 6 in particular. Similarly, results for several AVHRR cases on other dates around the airborne data acquisition day (August 6–10) differ from nominal values by varying amounts (Fig. 15).

Neither of the data sets from the small footprint satellite sensors was acquired on the same day as the airborne hyperspectral data acquisitions. For TM data acquired 4 days after the *casi* data acquisition (August 8), matches in the range of −2.7% to +8.7% were

obtained. The QUASAR results for SPOT-2 HRV on August 7 predict TOA radiances −5.4% to −2.4% lower than nominal radiances.

8.3. Results for the NCRA test site (October)

The QUASAR TOA radiance estimate for AVHRR on October 5 differs from the nominal value by −7.2%, similar to the result obtained on the airborne data acquisition day (October 4). The VGT results on October 3 are closer to nominal values than the VGT results on October 4, ranging from −6.8% to +10.9%. SeaWiFS cases on other dates around the airborne data acquisition day (October 5–8) differ increasingly from nominal values as a function of temporal extension (Fig. 15).

8.4. Discussion of temporal extension results

It is clear from the above results that temporal extensions of a few days do not necessarily provide calibration redundancy and may even create higher levels of uncertainty. The temporal trends obtained can be caused by changes in surface conditions, atmospheric conditions, and/or observation geometries affecting BRF adjustments, but little more can be said in the absence of ground-based measurements on these days.

An overview of the main QUASAR results (40 cases) and the temporal extension results (86 cases) is presented in Table 6. Absolute values of the relative differences between QUASAR and nominal TOA radiances were averaged to generate the excursions given in the table. On the left-hand side of the table, the averages are over the number of spectral band cases. On the right-hand side, the averages are weighted by the number of satellite sensor cases, which gives each satellite sensor equal weight regardless of the number of spectral band cases included in the results for that sensor. The table indicates that the RVPN test site yields lower relative excursions overall than does the NCRA test site, which is consistent with the higher radiances characteristic of the former. The table also indicates that the RVPN results change more with temporal extensions.

Based on Table 6, the average excursions for the main QUASAR results at the RVPN and NCRA test sites are in the 4–5% range and in the 8–10% range, respectively. Since these excursions are with respect to nominal calibration results, which have their own uncertainty, they are not a measure of the absolute error associated with the QUASAR approach. Nevertheless, the results are in keeping with the ±6% estimate of Scott et al. (1996) for cross-calibration using the Railroad Valley playa.

9. Concluding remarks

A new calibration monitoring methodology has been developed and tested at the RVPN and NCRA test sites.

QUASAR monitoring results have been generated for five satellite sensors based on airborne hyperspectral data acquisition campaigns at the Railroad Valley playa test site in Nevada in June 1998 and the Newell County rangeland test site in Alberta in August and October 1998. The main results consist of AVIRIS-based and *casi*-based TOA radiance predictions and their percentage difference comparisons with satellite image-based TOA radiances determined independently using nominal post-launch calibration coefficients.

Field measurements and remote sensing data processing results based on the chosen sensor set for experimental QUASAR monitoring (Microtops-II, GER3700, and *casi*) were validated against independent sensor results at the RVPN test site (Reagan, FieldSpec, and AVIRIS). Consistent results were obtained in all cases except for *casi*-based QUASAR reflectances, which indicated a *casi* radiometric calibration problem. A calibration correction was generated using the AVIRIS:*casi* reflectance ratio for the RVPN test site in order to correct the *casi*-based QUASAR results obtained at the NCRA test site.

For QUASAR monitoring based on the same-day reference data set for the RVPN test site, there is good agreement between QUASAR-based and nominal TOA radiances, with average excursions from nominal in the range of 4–5% (relative). For 12 spectral band cases, the TOA radiance comparison is characterized by a slope of 1.08 and a coefficient of determination (r^2) of .95. Compared to the RVPN results, there is less agreement between QUASAR-based and nominal TOA radiances for the NCRA test site, with average excursions from nominal in the range of 8–10% (relative). For 28 spectral band cases, the TOA radiance comparison is characterized by a slope of 0.81 and r^2=.87. For the combined results from the RVPN and NCRA test sites (40 spectral band cases), the general agreement between QUASAR-based and nominal TOA radiances is characterized by a slope of 1.03 and r^2=.99. Thus, while the NCRA results have apparently inferior statistics, the use of the lower-radiance rangeland test site improves the TOA radiance comparison that constitutes the main QUASAR monitoring result. The collective results also indicate that the nominal on-orbit radiometric calibrations of all the satellite sensors fit within their predicted uncertainties.

Based on the 40 spectral band cases examined, the QUASAR approach is not sensitive in any systematic way to wavelength, illumination and observation angles, and BRF adjustment factor. The main source of error is very likely inadequate knowledge of the surface BRF. The use of a rangeland test site for QUASAR monitoring will require better characterisation of surface reflectance anisotropies.

Temporal extensions of QUASAR data sets to days near to the airborne data acquisition day yield mixed results. The RVPN results are more affected by temporal extensions than are the NCRA results. In general, one must be wary of the trade-off between calibration data redundancy offered by temporal extensions and validation degradation induced by significant day-to-day changes in test site conditions.

Overall, the results obtained to date are sufficiently promising that, with careful refinements, the QUASAR methodology has the potential to become a generalized approach to vicarious calibration. The approach constitutes a worthwhile validation exercise that generates useful and informative radiometric calibration redundancy when applied to a number of Earth observation satellite sensors. In due course, QUASAR benchmark data sets have the potential to benefit commercial data providers by facilitating quality control procedures used with their data products and algorithms. Applications requiring consistency of multi-temporal and multi-sensor data sets should also be beneficiaries. While helping to monitor the status of satellite sensors internationally, the research and development activity also advances hyperspectral data acquisition and analysis techniques. In addition, the QUASAR approach is sufficiently general that it could in time be extended to the generation of validation data sets for the monitoring of biogeophysical parameters.

9.1. Future work

Recommended future activities include post-launch QUASAR monitoring tests for large footprint sensors such as MODIS, MERIS, and GLI, and small footprint sensors such as Landsat-7 Extended Thematic Mapper Plus (ETM+), ASTER, and EO-1 sensors, among others. MODIS is of particular interest in this respect because of its extensive onboard sensor calibration systems. The extension of the QUASAR monitoring approach to the SWIR will be important since many future sensors will have bands in this spectral region. Additional radiometric uniformity studies of the RVPN and NCRA test sites and completion of a full radiometric error model and analysis for the QUASAR method are high priorities.

Despite the desire for a simple and robust program of test site monitoring, there are several research questions and issues to be addressed. Most importantly, an improved understanding of the test sites will require proper characterization of their directional reflectance properties as a function of location and season. BRF models for each test site are needed as part of the QUASAR data processing and analysis and, moreover, any surface spectral reflectance maps produced for a test site should ultimately include a BRF model as part of the benchmark data set. Several campaigns of airborne coverage by multi-directional sensors such as POLDER (Polarization and Directionality of the Earth's Reflectances) and/or ASAS (Advanced Solid-state Array Spectroradiometer) would go a long way towards addressing this issue, although there are no specific plans in this regard. An evaluation of the impact of directional reflectance properties on the accuracy of the QUASAR

method will be facilitated by the completion of the error budget model.

Other research questions that require attention include the following. How accurately do test site locations have to be determined in satellite imagery? What is the optimum balance between good surface uniformity and the minimum area extent needed for each test site to accommodate large footprint sensors of interest? Is test site radiometry at finer spatial scales sufficiently uniform for vicarious calibration of smaller footprint sensors? What are the finest spatial and spectral resolutions needed for the reference hyperspectral imagery? What spatial and spectral sampling techniques should be used to simulate the various types of satellite data based on the reference hyperspectral imagery? How does the QUASAR monitoring method compare to independent vicarious calibration techniques?

Acknowledgments

References

Bergeron, M., O'Neill, N. T., Royer, A., & Teillet, P. M. (1998). Development of a spectral error model for surface bidirectional reflectance factor (BRF) retrieval. *Canadian Journal of Remote Sensing*, *24* (2), 128–132.

Biggar, S. F., Slater, P. N., & Gellman, D. I. (1994). Uncertainties in the in-flight calibration of sensors with reference to measured ground sites in the 0.4 to 1.1 mm range. *Remote Sensing of Environment*, *48*, 242–252.

Biggar, S. F., Slater, P. N., Thome, K. J., Holmes, A. W., & Barnes, R. A. (1993). Preflight solar-based calibration of SeaWiFS. In: *Proceedings of SPIE Conference, 1939*, (pp. 233–242).

Cabot, F., Hagolle, O., Ruffel, C., & Henry, P. (1999). Use of a remote sensing data repository for in-flight calibration of optical sensors over terrestrial targets. In: *Proceedings of the SPIE Conference on Earth Observing Systems IV, SPIE, vol. 3750* (pp. 514–523) Denver, CO.

Chen, J. M., & Cihlar, J. (1997). A hotspot function in a simple bidirectional reflectance model for satellite applications. *Journal of Geophysical Research*, *102* (D22), 25907–25913.

Dinguirard, M., & Slater, P. N. (1999). Calibration of space-multispectral imaging sensors: a review. *Remote Sensing of Environment*, *68* (3), 194–205.

Fu, G., Baith, K. S., & McClain, C. R. (1998). SeaDAS: the SeaWiFS data analysis system. In: *Proceedings of the 4th Pacific Ocean Remote Sensing Conference* (pp. 73–77). Qingdao, China.

Guenther, B., Barnes, W., Knight, E., Barker, J., Harnden, J., Weber, R., Roberto, M., Godden, G., Montgomery, H., & Abel, P. (1996). MODIS calibration: a brief review of the strategy for the at-launch calibration approach. *Journal of Atmospheric and Oceanographic Technology*, *13* (2), 274–285.

Nandy, P., Thome, K. J., & Biggar, S. F. (1998). Instrument for the retrieval of BRDF data for vicarious calibration. In: *Proceedings of the 1998 IEEE International Geoscience and Remote Sensing Symposium (IGARSS'98), vol. II,* (pp. 562–564). Seattle, WA.

Nandy, P., Thome, K. J., & Biggar, S. F. (1999). Laboratory characterization of a CCD camera system for retrieval of bidirectional reflectance distribution function. In: *Proceedings of SPIE Europto Conference — Sensors, Systems and Next Generation Satellites V, SPIE vol. 3870*; (pp. 234–242) Florence, Italy.

Neville, R. A., Rowlands, N., Marois, R., & Powell, I. (1995). SFSI: Canada's first airborne SWIR imaging spectrometer. *Canadian Journal of Remote Sensing*, *21* (3), 328–336.

Roujean, J.-L., Leroy, M. J., & Deschamps, P.-Y. (1992). A bidirectional reflectance model of the Earth's surface for the correction of remote sensing data. *Journal of Geophysical Research*, *98*, 20455–20468.

Santer, R. P., Schmechtig, C., & Thome, K. J. (1996). BRDF and surface-surround effects on SPOT-HRV vicarious calibration. In: *Proceedings of SPIE Europto Conference, SPIE, vol. 2960.* (pp. 344–354).

Scott, K. P., Thome, K. J., & Brownlee, M. R. (1996). Evaluation of the Railroad Valley playa for use in vicarious calibration. In: *Proceedings of SPIE Conference 2818*, Denver, CO.

Slater, P. N., Biggar, S. F., Holm, R. G., Jackson, R. D., Mao, Y., Moran, M. S., Palmer, J. M., & Yuan, B. (1987). Reflectance- and radiance-based methods for the in-flight absolute calibration of multispectral sensors. *Remote Sensing of Environment*, *22*, 11–37.

Slater, P. N., Biggar, S. F., Palmer, J. M., & Thome, K. J. (1996). Unified approach to absolute radiometric calibration in the solar-reflective range. In: *Proceedings of SPIE Europto Conference*, (16 pp.) Taormina, Italy.

Slater, P. N., Biggar, S. F., Thome, K. J., Gellman, D. I., & Spyak, P. R. (1996). Vicarious radiometric calibrations of EOS sensors. *Journal of Atmospheric and Oceanic Technology*, *13*, 349–359.

Staenz, K., Szeredi, T., & Schwarz, J. (1998). ISDAS — a system for processing/analyzing hyperspectral data. *Canadian Journal of Remote Sensing*, *24* (2), 99–113.

Staenz, K., & Williams, D. J. (1997). Retrieval of surface reflectance from hyperspectral data using a look-up table approach. *Canadian Journal of Remote Sensing*, *23* (4), 354–368.

Tanre, D., Deroo, C., Duhaut, P., Herman, M., Morcrette, J. J., Perbos, J., & Deschamps, P. Y. (1990). Description of a computer code to simulate the satellite signal in the solar spectrum: the 5S code. *International Journal of Remote Sensing*, *11*, 659–668.

Teillet, P. M. (1997). A status overview of Earth observation calibration/validation for terrestrial applications. *Canadian Journal of Remote Sensing*, *23* (4), 291–298.

Teillet, P. M., Fedosejevs, G., & Gauthier, R. P. (1998). Operational radiometric calibration of broadscale satellite sensors using hyperspectral airborne remote sensing of prairie rangeland: first trials. *Metrologia*, *35*, 639–641.

Teillet, P. M., Fedosejevs, G., Gauthier, R. P., & Schowengerdt, R. A. (1998). Uniformity characterization of land test sites used for radiometric calibration of Earth observation sensors. In: *Proceedings of the Twentieth Canadian Symposium on Remote Sensing*, (pp. 1–4) Calgary, Alberta.

Teillet, P. M., Horler, D. N. H., & O'Neill, N. T. (1997). Calibration, validation, and quality assurance in remote sensing: a new paradigm. *Canadian Journal of Remote Sensing*, *23* (4), 401–414.

Teillet, P. M., Slater, P. N., Ding, Y., Santer, R. P., Jackson, R. D., & Moran, M. S. (1990). Three methods for the absolute calibration of the NOAA AVHRR sensors in-flight. *Remote Sensing of Environment*, *31*, 105–120.

Thome, K., Markham, B., Barker, J., Slater, P., & Biggar, S. (1997). Radiometric calibration of Landsat. *Photogrammetric Engineering and Remote Sensing*, *63* (7), 853–858.

Vermote, E. F., & Kaufman, Y. J. (1998). Absolute calibration of AVHRR visible and near-infrared channels using ocean and cloud views. *International Journal of Remote Sensing*, *16* (13), 2317–2340.